Geophysical Journal International

*Geophys. J. Int.* (2024) **236,** 1577–1595
Advance Access publication 2023 December 19
GJI Geomagnetism and Electromagnetism

https://doi.org/10.1093/gji/ggad479

# Characterization and imaging magnetic minerals from ultramafic roots of a LIP: implication for deep crustal magnetic sources

Geertje W. ter Maat [1], Nathan S. Church [1], Hirokuni Oda,[2] Zeudia Pastore[1] and Suzanne A. McEnroe [1]

[1] *Department of Geoscience and Petroleum, Norwegian University of Science and Technology (NTNU), 7031 Trondheim, Norway. E-mail: geertjetermaat@gmail.com*
[2] *Geological Survey of Japan, National Institute of Advanced Industrial Science and Technology (AIST), Tsukuba, Ibaraki 305-8560, Japan*

Accepted 2023 October 31. Received 2023 October 25; in original form 2023 February 21

## SUMMARY

Satellite magnetic surveys have revealed features consistent with magnetization at depth in the lithosphere. Previous studies have reported magnetic minerals preserved in mantle nodules and in some eclogite facies rocks. Deep crustal rocks are another possible source for these deep lithospheric signals, but have not been extensively studied, in many cases due to the difficulty in obtaining samples unaffected by later near-surface alteration processes. Here, we used a combined approach involving petrophysical, rock magnetic and scanning magnetic microscopy (SMM) analyses on unaltered pristine ultramafic samples from the Reinfjord Ultramafic Complex in northern Norway. The focus was to identify the magnetic carriers using SMM and link the magnetic anomalies mapped in thin section to distinct rock magnetic measurements. The dominant magnetic carriers are Cr-magnetite exsolved from grains of Al-chromite, and magnetite exsolution lamellae from clinopyroxene. In addition, some samples have exsolved magnetite from Al-Cr-spinel and Fe-rich exsolution from Cr-spinel as carriers. Rock magnetic measurements suggest that these primary magnetic carriers, could retain magnetization to considerable crustal depths.

**Key words:** Magnetic properties; Microstructure; Magnetic mineralogy and petrology; Rock and mineral magnetism; Large igneous provinces.

## 1 INTRODUCTION

Magnetic field anomalies result from the combined response of magnetic minerals to the present Earth's field and their remanent (permanent) magnetization. In magnetic surveys, the type of information obtained is directly related to the distance from the source rock to the magnetometer. From satellite measurements operating on planetary crustal scales to scanning magnetic microscopy (SMM) at the micron scale, anomaly data are broadly used to understand the magnetic lithosphere, to map geological structures, to reconstruct tectonic plate motion, to explore for natural resources and to identify mineral sources of magnetization.

It is nearly 50 yr since the first magnetic anomaly map of the lithosphere was produced based on POGO satellite data (Regan *et al.* 1975). The later Ørsted and CHAMP missions produced more detailed magnetic data, and the latter in combination with aeromagnetic and submarine data was used to create the World Digital Magnetic Anomaly Map (Korhonen *et al.* 2007). More precise data of the field are currently being collected by the three SWARM satellites (Sabaka *et al.* 2020). These satellite data sets spurred research on the magnetic properties of the lithosphere (Schlinger 1985, 2001; Kelso *et al.* 1993; McEnroe *et al.* 1996, 2001a,b, 2004a, b, 2018; Pilkington & Percival 2001; Brown & McEnroe 2008; Schmidt *et al.* 2007; Dunlop *et al.* 2010; Brown *et al.* 2011; Liu *et al.* 2012; ter Maat *et al.* 2019). Recent work on mantle nodules (Ferré *et al.* 2014, 2021) supports the argument that upper-mantle rocks can hold strong components of remanent magnetization and substantially contribute to lithospheric magnetic anomalies. However, the extent to which lower crustal rocks also may be sufficiently magnetic to contribute to long-wavelength anomalies remains unanswered (Purucker & Clark 2011; Purucker & Whaler 2015; McEnroe *et al.* 2018).

Directly characterizing the mineral sources of magnetic anomalies is a challenge, particularly when the larger assemblage formed and equilibrated in deep lithospheric conditions. To assess the magnetic contributions of deep-seated rocks *in situ*, it is necessary to ascertain whether the magnetic mineral source is primary or is a later mineral phase created by secondary processes, such as serpentinization in ultramafic rocks (Michels *et al.* 2018; Yu & Tikoff 2020), or retrograde metamorphism in uplifted rocks. Differentiating the magnetic phases produced by these processes from the original oxides requires an interdisciplinary approach combining mineralogy, petrology and rock magnetism (Pastore *et al.* 2018b). Commonly, surface exposures of ultramafic dunite–pyroxenite–wehrlite rocks

are altered by serpentinization, which produces magnetite and may overprint the original source of magnetization. In such processes the primary magnetic oxides can be destroyed, or new magnetic oxides formed (Clark 1997, 1999).

Other than composition, the dominating factor on the stability of crustal magnetization is temperature ($T$), and hence the depth to the Curie isotherm of 580 °C for pure magnetite, assuming no pressure effect. Above this temperature, magnetite is paramagnetic, losing both induced and remanent magnetic components and therefore does not contribute to long-wavelength anomalies. The depth at which this magnetic phase transition occurs depends on the thermal gradient. The magnetization of cold cratonic crust will be maintained to deeper levels than in areas of high heat flow. Experimental work on magnetite indicates a minor increase in Curie $T$ with pressure of approximately 2 °C kb$^{-1}$ or 20 °C per 10 kb, with a lesser effect in magnetite containing Ti in solid solution (Schult 1970; Gilder *et al.* 2004; Gilder & LeGoff 2008; Kupenko *et al*. 2019). Experimentally the effect of pressure is difficult to fully assess because measurements must be made simultaneously at both the pressures and temperatures of interest, and on a range of compositions and microstructures.

Here, we focus on ultramafic cumulates considered to represent the deep roots of a large igneous province (Grant *et al.* 2016, 2020). Our aim is to understand the nature of the magnetic minerals and microstructures, and their magnetic properties. We map the magnetic phases using SMM to determine the primary and secondary magnetic signals and isolate their magnetic properties further through rock magnetic measurements. By combining these datasets, we contribute to the unanswered questions from large-scale magnetic surveys of the deeper crust, the possible magnetic contributions from deep-seated unaltered ultramafic bodies and the nature of primary magnetic phases in ultramafic cumulates.

## 2 GEOLOGICAL SETTING

The Reinfjord Ultramafic Complex (RUC) is part of the 5000 km$^2$ Seiland Igneous Province (SIP) in northern Norway and is considered to represent one of the roots of this Large Igneous Province (LIP). The RUC formed as a magmatic conduit system at 25–35 km depth, at temperatures of at least 1400 °C (Bennett *et al.* 1986; Griffin *et al.* 2013; Pastore *et al.* 2016, 2018a) and pressures of 6.8–9 kb (Grant *et al.* 2016, 2020). The RUC was emplaced in a time interval of 580–569 Ma (Larsen *et al*. 2018). The ultramafic rocks intruded in three successive events resulting in a Lower Layered Series (LLS), an Upper Layered Series (ULS) and the Central Series (CS) formations. The LLS, ULS and CS are composed of ultramafic cumulates, ranging from pyroxenite-wehrlite to dunite.

Larsen *et al.* (2018), Grant *et al.* (2020) and Ryan *et al.* (2022) provide a recent overview of the complex petrogenesis of the RUC, detailing the modal layering of the Upper Layered Series and variations in olivine composition in the CS and the crosscutting pyroxenite dykes representing the final stage of the emplacement of the ultramafic formations.

Where the ultramafic rocks intruded the host rock, hybrid marginal zones formed, with bulk compositions depending on the intermingling of the melted host rock and intruding ultramafic composition. In the RUC, the Marginal Zone rocks (MZ) are the contact zones between gabbro and ULS or CS. Later five generations of ultramafic or mafic dykes crosscut all lithologies. Though there are areas of localized serpentinization due to faulting and related fluid flow, parts of the RUC have only minor alteration. Ter Maat *et al.* (2019) provides a description of the petrophysical properties from 667 specimens collected from surface locations (108 samples) and from two deep drill cores of 391 and 348 m long. Based on petrographic observations and petrophysical measurements they concluded that a subset of their samples were pristine unaltered ultramafic samples These samples all have high densities (>3.2 g cm$^{-3}$), a feature expected from ultramafic rocks which have not been serpentinized. However, these samples have a wide range in NRM and susceptibility values, which were correlated to the size and abundance of magnetic oxides and their microstructures. Because these oxide phases could represent a source of magnetization in the lower crust a subset of these pristine ultramafic samples is further investigated here. A geological map of the RUC (Fig. 1) shows the five site locations for the samples discussed in this paper.

## 3 METHODS

Transmitted- and reflected-light, and electron microscopy was used to examine the mineral assemblages and oxide mineral microstructures of the ultramafic cumulates. Scanning electron microscopy images were obtained in backscattered electron (BSE) mode. To acquire compositional estimates of the oxides we used energy-dispersive spectroscopy (EDS) at a working distance of 4 mm and 15 kV accelerating voltage using a FEI Helios G4 Dual-beam FIB-SEM at the NTNU Nanolab facility. Additional BSE images were acquired using a Phenom tabletop SEM.

Magnetic hysteresis loops, backfield remanence curves and first-order reversal curves (FORCs) were measured using a Princeton Measurements Corp. vibrating sample magnetometer (VSM) on 5–30 mg sample chips from 6 samples per site. Hysteresis parameters and backfield curves were measured for at least one sample per site using a 1 T saturating field. FORCs were measured for seven selected samples at a saturating field of 1.0 T and a field increment of 2.5–4 mT. The FORCs were processed using FORCinel 3.0 (Harrison & Feinberg 2008) with the VARIFORC technique (Egli 2013) using smoothing factors of 12–24.

Thermomagnetic measurements were made using three methods. Low- and high-temperature measurements were carried out on an AGICO MFK1 Kappabridge from −192 to 700 °C. Additional low-temperature measurements were made in a Quantum Design Magnetic Properties Measurement System (MPMS). Samples were cooled to 20 K in a 2.5 T field and measured during warming to 300 K (FC), then cooled in zero field to 20 K where a 2.5 T field was imparted and magnetization was measured on warming to room temperature (ZFC).

Further high-temperature measurements on rock chips were made in the VSM with a flowing helium furnace following the method of Fabian *et al.* (2013) which uses sequences of initial magnetization curves. At each step the sample is heated while the field is increased in 20 mT steps to a maximum field of 1 T. Subsequent processing calculates the saturation magnetization ($M_s$), saturation remanence ($M_{rs}$) and high- and low-field susceptibility from room temperature to 700 °C. The temperature was increased with a step size of 2 °C, and the measurement time for the initial curves were 12 s.

For the identification of magnetic remanence carriers SMM of thin sections were made using a scanning SQUID microscope (Oda *et al*. 2016) at the Geological Survey of Japan, National Institute of Advance Industrial Science and Technology (AIST). In addition, one sample (S8e) was measured on a scanning magnetic tunnel junction (MTJ) instrument at the NTNU Rock- and Palaeomagnetic laboratory (Church & McEnroe 2018). In both cases the vertical

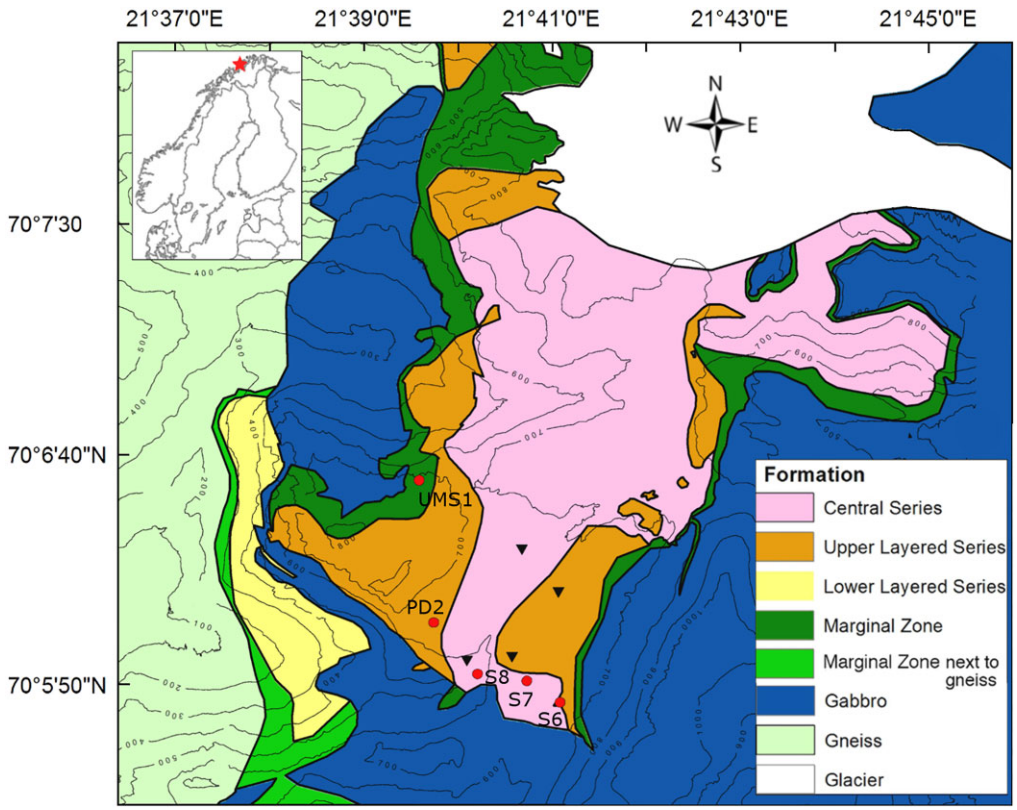


**Figure 1.** Geological map of the Reinfjord Ultramafic Complex with 100 m interval contours of topography (LIDAR data/Norwegian Mapping Authority). Red dots indicate sample site locations for this study. Black triangles indicate drill core locations as described in ter Maat *et al.* (2019). The inset map shows the location of the complex on the map of Fennoscandia.

component of the field was measured at room temperature in field-free conditions. The SQUID microscope has a 200 × 200 μm$^2$ washer type pickup coil, and a field resolution of 1.1 pT $(\sqrt{(\text{Hz})})^{-1}$ at 1 Hz (Kawai *et al*. 2016), and scans were acquired at a sensor-to-sample distance of 275–286 μm, except for sample S8e, where the distance was increased to ∼1 mm due to its strong magnetization. The MTJ instrument has a field noise of ∼70 nT $(\sqrt{(\text{Hz})})^{-1}$ at 1 Hz, the S8e scan was acquired with the sensor tip 150 μm above the sample.

## 4 RESULTS

Based on the initial petrophysical properties of 467 ultramafic samples (ter Maat *et al.* 2019), five samples from the ultramafic cumulates and cogenetic intrusives at the centre of the RUC were selected for a SMM mineralogical and detailed rock-magnetic study.

Later processes that alter the high-pressure, high-temperature ultramafic assemblages such as serpentinization will result in lowering the bulk densities due to the replacement of high-density olivine or pyroxene by lower-density secondary minerals such as serpentine. The density value of 3.2 g cm$^{-3}$ was used as a cut-off for pristine samples by ter Maat *et al.* (2019) and all samples used in this study all have mean densities above this value (Fig. 3; Table 1). Further, thin-section analysis indicated no evidence for later alteration, or serpentinization.

The five selected samples are from the ultramafic-country rock marginal zone (UMS1j), pyroxenite dykes cross-cutting the ULS (PD2b), the ULS (S6f) and two CS dunite samples, one with strong magnetization (S8e), one with a weak magnetization (S7c).

### 4.1 Petrography

The petrography of the ultramafic rocks in the RUC is described by Bennett *et al.* (1986), Grant *et al.* (2016) and ter Maat *et al.* (2019). Here, we focus on the selected thin sections for which magnetic scans were obtained. The CS dunite samples (S7 and S8) are both dominated by olivine (>90 per cent) with minor amounts of orthopyroxene, clinopyroxene and spinels. A major distinction between samples S8 and S7 is the size of the olivine grains with diameters up to 1–2 cm in S8, while in S7 olivine grains have a maximum diameter of 1.5 mm. Both thin sections contain abundant interstitial opaque minerals, with S8 containing fewer, but larger grains up to several tens of microns and S7 containing more numerous, but smaller, grains (<10 um). The ULS site, S6, contains abundant olivine, clinopyroxene with exsolved lamellae of orthopyroxene and oxide and discrete opaque grains.

The dominant oxides in the CS dunites and the layered series are shown in Figs 2(b)–(d). The typical oxides in the CS rocks are chromium-rich spinels, one with very fine and sparse exsolution of an iron-rich phase, and one with abundant exsolution (Fig. 2). Both spinels are found in association with ilmenite (Fig. 2b). A ternary classification diagram of the composition of the spinel grains in site S7 and S8, determined by EDS analysis, is given in Fig. 2(a). Using the classification of Stevens (1944), the host spinel with fine exsolution microstructures found in the weakly magnetic S7 sample is designated as Fe-poor Al-Cr-spinel. The fine exsolution blebs range in size from micron to submicron size and resulted in overlap analyses, however analyses indicate strong Fe-enrichment in the exsolution blebs compared to the host. Here, these exsolution blebs commonly form as spherical or blob-like textures. The spinel in

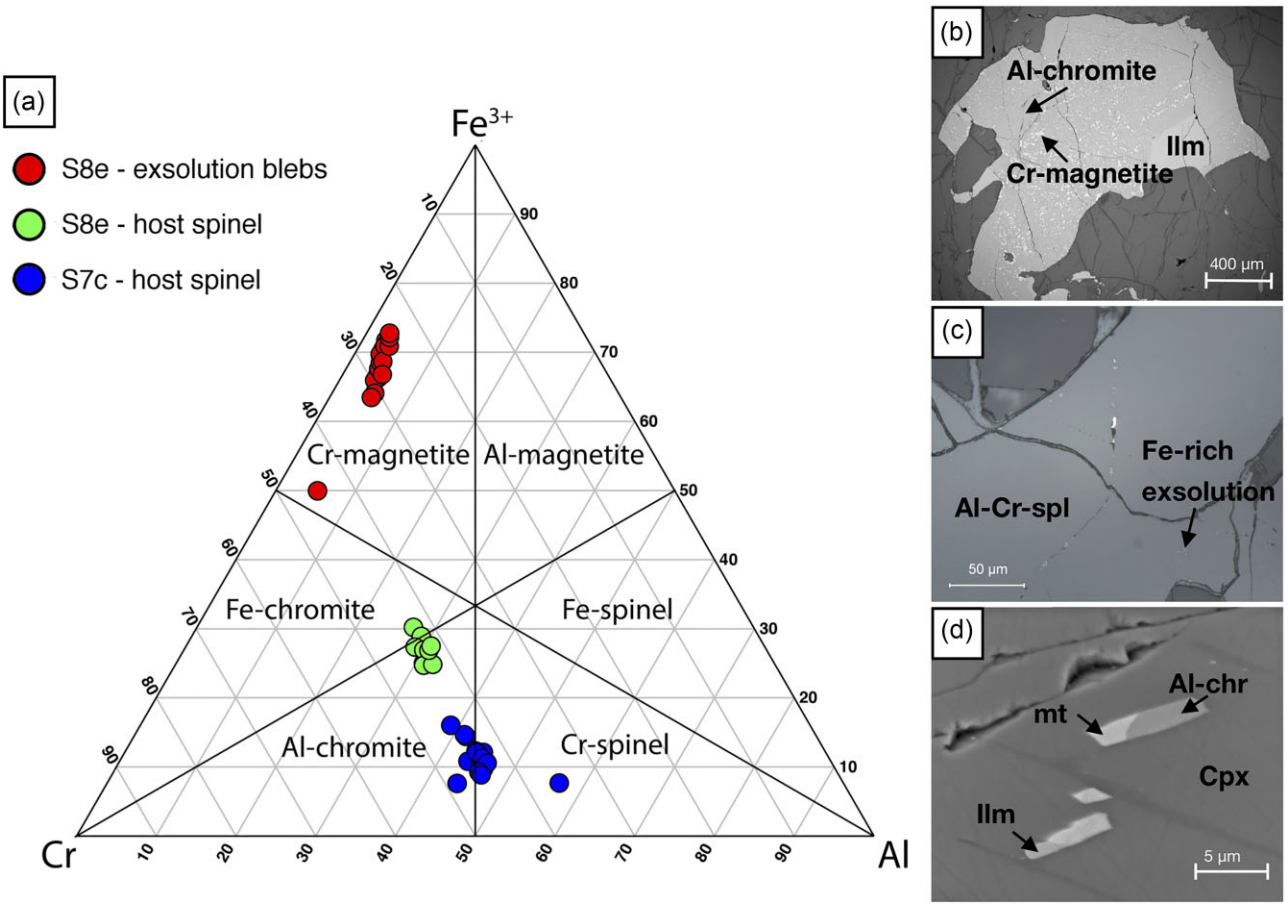


**Figure 2.** Ternary classification diagram ($Cr^{3+}$,$Fe^{3+}$,$Al^{3+}$): $Y(Cr^{3+})=Cr/(Cr + Fe^{3+}+Al)$; $Y(Fe^{3+})=Fe^{3+}/(Cr + Fe^{3+}+Al)$; $Y(Al^{3+})=Al/(Cr + Fe^{3+}+Al)$. Regions as defined by Stevens (1944). EDS analysis results on spinel grains in S7c and S8e are plotted. For S8e the host and exsolved phase were analysed; for S7c only the host composition is plotted. The exsolved phase in S8 is Cr-magnetite, the host consists of Fe-rich Al-chromite. The host spinel in S7c plots in both the Fe-poorer Al-chromite and Cr-spinel and will be referred to as Al-Cr-spinel. (b–c) backscattered electron images of the oxides phases in samples S8e (b) and S7c (c). (d) backscattered electron image of exsolution lamellae of magnetite, Al-chromite and ilmenite from clinopyroxene in sample S6e.

sample S8, with abundant exsolution contains more iron, and the host is as designated as Al-chromite, and the exsolved phases as Cr-magnetite (Fig. 2). The exsolved Cr-magnetite blebs from Al-chromite are randomly distributed throughout the host with varying sizes from submicron to over 40 µm in diameter, which are subhedral and irregular in shape. This spinel assemblage is found in both S8 and S6. Both host and exsolved Cr-magnetite blebs may contain further fine cloth-like microstructure.

Additional oxide phases are found in samples S6f (ULS) and S8e (CS). Site S6, and to lesser extent site S8, contain clinopyroxene with exsolved magnetite and ilmenite lamellae, and spinel (Fig. 2d). In site S8, abundant non-magnetic sulphides are present, mainly chalcopyrite, pyrite and pentlandite, and in one sample a pyrrhotite, pyrite and chalcopyrite assemblage is found in association with a Cr-spinel grain, which has very fine exsolution blebs (Fig. 9h).

Samples from the pyroxenite dyke (PD2) and marginal zone (UMS1) have a similar mineralogy. These contain clinopyroxene, olivine and orthopyroxene, and opaque grains. The clinopyroxene has varying amounts of exsolution lamellae of orthopyroxene, ilmenite, magnetite and Cr-spinel. The oxide mineralogy in the PD and MZ (samples PD2 and UMS1) are similar, with abundant exsolved magnetite lamellae in clinopyroxene and discrete magnetite grains. The magnetite grains are found at grain boundaries of olivine as inclusions in the silicates or distributed in a fine matrix. Additionally, orthopyroxene with oxide exsolution lamellae is present in the pyroxenite dyke sample (PD2).

### 4.2 Petrophysical properties

Samples reported here were measured for magnetic susceptibility ($\kappa$ , 248), NRM (246), density (257) and hysteresis properties (186). Fig. 3 shows a comparison between the selected samples, and their value with respect to the other samples of the same rock formation. Among these high-density samples, the susceptibility and NRM properties vary by over two orders of magnitude. To identify the origin of this variation in the CS, two sites were selected, one with high (S8) and one with low (S7) NRM and susceptibility values. Samples from site S7 show a large range of densities and limited variation in NRM and susceptibility values, whereas site S8 has a limited density range, but a greater variation in NRM and susceptibility. Site S6 is representative for the ULS, with similar site and formation means. The ULS is a layered formation with varying proportions of wehrlite and dunite, and consequent variations in the clinopyroxene-olivine ratio may be the origin of the large range in magnetic properties. Site S6 has a similar range in density to S7, however there is a larger variation in NRM and susceptibility

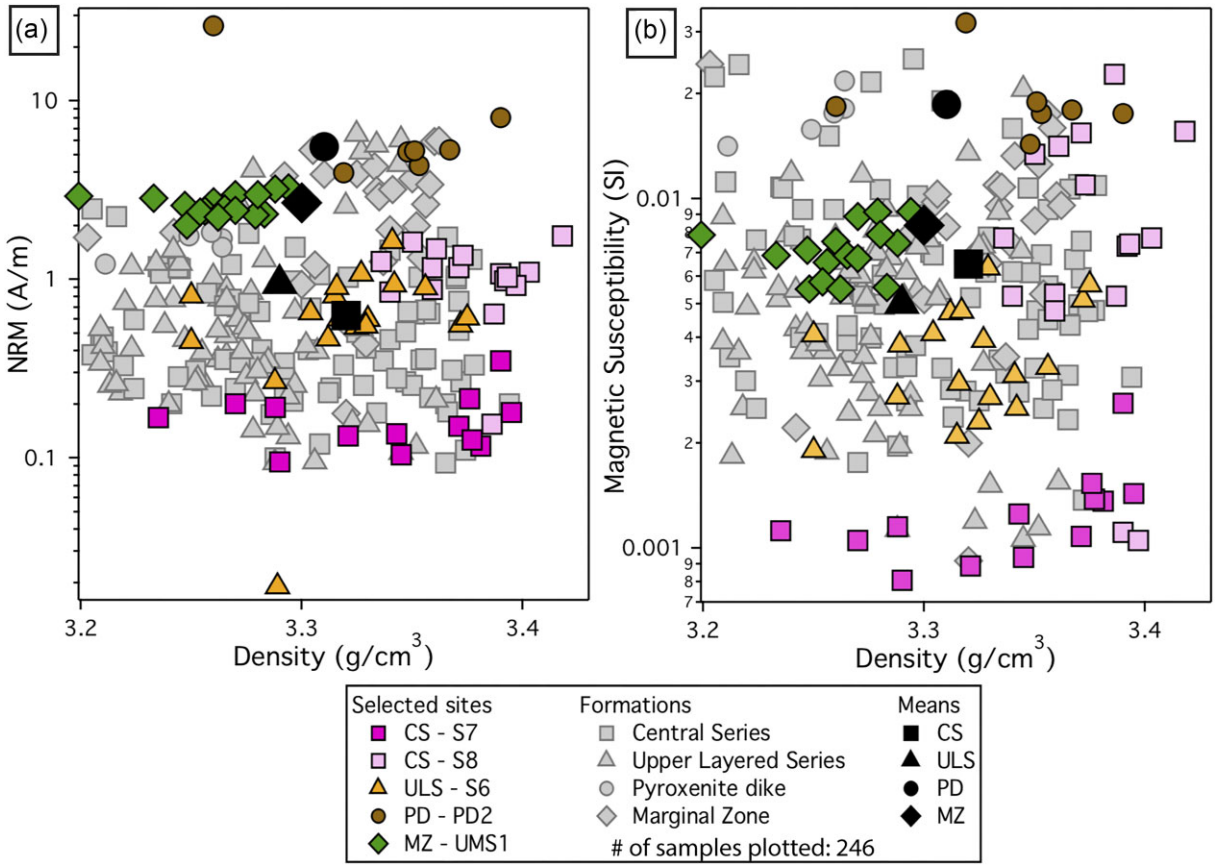


**Figure 3.** (a) NRM versus density and (b) susceptibility versus density for ultramafic and MZ samples with densities $>3.2$ g cm$^{-3}$. Four Symbols represent four formations. Coloured symbols are samples from 5 sites in this paper, grey shaded symbols are samples from same formation, and solid black symbols are formation means. [densities are reproduced from ter Maat *et al.* (2019)].

values. The sample has values close to the average of the formation. Pyroxenite dyke samples were collected from only two sites, which yielded similar site means. Site PD2, used here, has the highest site average NRM and susceptibility of all sites in the RUC.

Site UMS1 is representative of the Marginal Zone formation, with petrophysical properties close to the MZ formation means. The NRM and susceptibility values from site UMS1 are well clustered compared to the other 4 selected RUC sites.

Magnetic susceptibility and NRM determine the intensity, shape and polarity of crustal magnetic anomalies generated in Earth's field. The relative contribution remanence to the magnetization induced by the geomagnetic field ($M_i$, A m$^{-1}$) is given by the Koenigsberger or $Q$ ratio $Q = NRM/M_i$, where $M_i = \kappa \times H$ and $H$ is the local field, here 42.5 A m$^{-1}$; (IGRF-2012; Thébault *et al.* 2015). ter Maat *et al.* (2019) reported that 63 per cent of all RUC samples have Koenigsberger ratios above 2, indicating that the remanent magnetization is twice as large as the induced. The median Q values for the pristine samples alone range from 1.9 for the CS to 8.1 for the marginal zone (Table 1). Of the sites that are the focus of this study, the CS sites have similar median values of 3.4 and 3.1 for strongly magnetic samples S8 and weak S7, respectively, both of which are higher than the median of the unit as a whole. The S6 and PD2 site medians are similarly higher than the total pristine unit values, with Koenigsberger ratios of 4.0 for the ULS and 7.0 for the pyroxenite dyke. By contrast, the $Q$ value for UMS1 is 8.6, which is close to the median for all pristine marginal zone samples of 8.1.

### 4.3 Magnetic hysteresis properties

Room-temperature hysteresis behaviour is controlled by the domain state and magnetic mineralogy. Hysteresis loops provide the parameters saturation remanence ($M_{rs}$), saturation magnetization ($M_s$) and coercivity ($H_c$) and additional backfield curves provide the coercivity of remanence ($H_{cr}$). The hysteresis parameter values are reported in Table 1.

The average magnetic domain state allows the remanence-carrying capacity of the sample to be inferred, however, most samples consist of magnetic mixtures, and this average domain state represents the bulk domain state. Commonly, the ratio $M_{rs}/M_s$ is plotted again the ratio $H_{cr}/H_c$ on a Day plot (Day *et al.* 1977). Roberts *et al.* (2018, 2019) state that bulk magnetic parameters are not specific enough to be used for domain state identification in magnetic mixtures. Tauxe *et al.* (2002) argue that the use of the ratio $H_{cr}/H_c$ is problematic as $H_{cr}$ behaves poorly for particles with magnetizations at large angles to the magnetic field, the authors recommend the use of the older squareness-coercivity plot (Néel 1955). Thus, both a Day plot (Fig. 4a) and a squareness-coercivity plot (Fig. 4b), which displays the ratio $M_{rs}/M_s$ ('squareness') against $H_c$ are compared. The site mean squareness and mean coercivity are similar for S7 and S8 and are higher than the CS formation means (black square; Fig. 4). Samples from site S6 have lower $H_c$ and squareness values compared to the formation mean (black triangle; Fig. 4), indicating a coarser magnetic grain fraction in the sample than in the rest of the formation. Site PD2 has squareness and coercivity values which are close to the Pyroxenite dyke formation

**Table 1.** Mean and median rock magnetic properties of the 246 pristine samples of the CS, ULS, PD and MZ, formations including the five selected sites. Number of sample measurements varies per property: susceptibility (248), NRM (246), density (257) and hysteresis (186). Calculated volume percentage magnetite from susceptibility, and from $M_s$ The Koenigsberger ratio ($Q$) is the ratio of the NRM to the induced magnetization ($M_i$ in A m$^{-1}$).

| | NRM | $\chi$ | $M_i$ | $Q$ | Density | $H_c$ | $M_{rs}$ | $M_s$ | $H_{cr}$ | $M_{rs}/M_s$ | $H_{cr}/H_c$ | Volume % mgt [per cent] from $\chi$ | Volume % mgt [per cent] from $M_s$ |
|---|---|---|---|---|---|---|---|---|---|---|---|---|---|
| | [A m$^{-1}$] | [SI] | [A m$^{-1}$] | | [g cm$^{-3}$] | [mT] | [mAm$^2$ kg$^{-1}$] | [mAm$^2$ kg$^{-1}$] | [mT] | | | | |
| Central Series (CS) | | | | | | | | | | | | | |
| Mean | 0.63 | 0.0065 | 0.275 | 2.29 | 3.32 | 13.67 | 42.1 | 231,5 | 30.08 | 0.18 | 2.2 | 0.182 | 0.16 |
| Median | 0.405 | 0.005 | 0.213 | 1.9 | 3.34 | 13.02 | 27.7 | 164.1 | 29.21 | 0.17 | 2.24 | 0.143 | 0.112 |
| S7 | | | | | | | | | | | | | |
| Mean | 0.167 | 0.0013 | 0.054 | 3.08 | 3.34 | 18.54 | 7.2 | 27.7 | 34.19 | 0.26 | 1.84 | 0.037 | 0.03 |
| Median | 0.151 | 0.0011 | 0.049 | 3.1 | 3.35 | 19.77 | 6.8 | 25.9 | 32.55 | 0.26 | 1.65 | 0.033 | 0.028 |
| S8 | | | | | | | | | | | | | |
| Mean | 1.091 | 0.0091 | 0.385 | 2.83 | 3.38 | 19.32 | 72.4 | 329.7 | 39.37 | 0.22 | 2.04 | 0.261 | 0.232 |
| Median | 1.087 | 0.0076 | 0.321 | 3.38 | 3.38 | 17.95 | 52.7 | 229.6 | 35.81 | 0.23 | 2 | 0.218 | 0.162 |
| Upper Layered Series (ULS) | | | | | | | | | | | | | |
| Mean | 0.946 | 0.005 | 0.211 | 4.48 | 3.29 | 19.52 | 50.8 | 211.9 | 35.12 | 0.24 | 1.8 | 0.135 | 0.145 |
| Median | 0.535 | 0.0043 | 0.183 | 2.92 | 3.28 | 19.39 | 41.5 | 165.7 | 36.85 | 0.25 | 1.9 | 0.118 | 0.112 |
| S6 | | | | | | | | | | | | | |
| Mean | 0.686 | 0.0037 | 0.156 | 4.4 | 3.32 | 14.72 | 27 | 143.6 | 31.76 | 0.19 | 2.16 | 0.106 | 0.1 |
| Median | 0.605 | 0.0035 | 0.151 | 4.01 | 3.33 | 14.15 | 21 | 100.8 | 30.29 | 0.21 | 2.14 | 0.102 | 0.07 |
| ULS Pyroxenite dyke (PD) | | | | | | | | | | | | | |
| Mean | 5.551 | 0.0186 | 0.792 | 7.01 | 3.31 | 11.94 | 108.2 | 835.1 | 32.52 | 0.13 | 2.72 | 0.496 | 0.58 |
| Median | 4.154 | 0.0178 | 0.755 | 5.5 | 3.32 | 12.44 | 125.2 | 961.3 | 28.41 | 0.13 | 2.28 | 0.507 | 0.673 |
| PD2 | | | | | | | | | | | | | |
| Mean | 8.368 | 0.0192 | 0.815 | 10.26 | 3.34 | 12.67 | 132.3 | 916.6 | 29.37 | 0.14 | 2.32 | 0.553 | 0.641 |
| Median | 5.26 | 0.0177 | 0.753 | 6.98 | 3.35 | 13.07 | 136.7 | 985.9 | 28.92 | 0.14 | 2.21 | 0.511 | 0.689 |
| Marginal Zone | | | | | | | | | | | | | |
| Mean | 2.685 | 0.0084 | 0.355 | 7.56 | 3.3 | 14.86 | 55.7 | 339.4 | 39.2 | 0.16 | 2.64 | 0.241 | 0.234 |
| Median | 2.599 | 0.0075 | 0.321 | 8.1 | 3.31 | 14.68 | 44 | 244.7 | 36.59 | 0.18 | 2.49 | 0.217 | 0.17 |
| UMS1 | | | | | | | | | | | | | |
| Mean | 2.639 | 0.0072 | 0.304 | 8.67 | 3.26 | 15.02 | 31.7 | 234 | 47.83 | 0.14 | 3.18 | 0.206 | 0.161 |
| Median | 2.542 | 0.007 | 0.297 | 8.55 | 3.26 | 16.57 | 18.5 | 104.3 | 51.42 | 0.18 | 3.1 | 0.202 | 0.071 |

mean. The mean $H_c$ value of the PD samples is the lowest of all the rock formations. UMS1 plots separate from the other MZ sites, with much lower squareness values than the Marginal Zone formation mean (black diamond; Fig. 4).

None of the samples contain titanomagnetite, yet most samples plot between the trend-lines of TM60 and low-Ti magnetite defined by Wang & van der Voo (2004). For the CS and ULS samples, which contain Al-chromite with Cr-magnetite as dominant carrier, this may indicate that the substitution of Fe by Cr has the same effect on the squareness and coercivity as the substitution of Fe by Ti. The samples from strongly magnetic S8 plot closer to the trend-line for low-Ti magnetite than those of S6 and weakly magnetic CS sample S7, which may reflect the contribution of Cr-poor magnetite in the former. The PD1 and UMS1 samples plot close to the trend of low-Ti magnetite, which is consistent with magnetite lamellae in clinopyroxene and discrete magnetite being the dominant magnetic carriers.

The variation in $M_s$ may be directly correlated to the amount of magnetic material in the sample. The volume per cent magnetite can be calculated from $M_s$ using the formula:

$$v\,(\%) = 100 \times M_{s\,(\mathrm{sample})}/M_{s\,(\mathrm{magnetite})},$$

where $M_{s\,(\mathrm{sample})}(\mathrm{A\,m^{-1}}) = \mathrm{Specific}\ M_s\ (\mathrm{Am^2\,kg^{-1}}) \times \mathrm{Density}_{\mathrm{sample}}\ (\mathrm{kg\,m^{-3}})$ and $M_{s\,(\mathrm{magnetite})} = 480\ 000\,\mathrm{A\,m^{-1}}$. The mean and median volume percentages based on this formula are given in Table 1. This formula assumes the magnetic mineral is pure magnetite. Nearly all samples fall above the trend-line for low-Ti magnetite in Fig. 4(b), indicating that most samples do not contain pure magnetite. Because the carrier is not end-member magnetite, a larger volume of magnetic material is required to account for the same magnetization in the above calculation. Therefore, we consider that the volume per cent magnetite for the Central and Upper Layered Series to be underestimated. Thus, the minimum volume percentages of 'magnetite' for sites S7, S8 and S6 are 0.138, 0.232 and 0.100, respectively. Sites from the Marginal Zone and Pyroxene dyke, UMS1 and PD2, contain end-member magnetite as the dominant magnetic carrier, and therefore the mean volume percentages of 0.395 and 0.641, respectively, are more accurate estimates.

To observe the differences in hysteresis shape, we plot the shape parameter $\sigma_{\mathrm{hys}}$ against the ratio median destructive field of remanence over the coercivity of remanence ($H_{\mathrm{rh}}/H_{\mathrm{cr}}$ Fig. 4c). The $H_{\mathrm{rh}}$ and $H_{\mathrm{cr}}$ are commonly similar, with $H_{\mathrm{rh}}$ higher than $H_{\mathrm{cr}}$ (Fabian & von Dobeneck 1997). The shape parameter $\sigma_{\mathrm{hys}}$ (Fabian 2003) is based on the area in the hysteresis loop ($E_{\mathrm{hys}}$) and the rectangular area of an ideal hysteresis loop with height $2 \times M_s$ and width $2 \times H_c$, which is defined as $\sigma_{\mathrm{hys}} = \ln(E_{\mathrm{hys}}/(4 \times M_s \times H_c))$. A wasp-waisted loop has an area larger than the ideal hysteresis loop ($\sigma_{\mathrm{hys}} > 0$) and a potbellied loop has an area smaller than the ideal one ($\sigma_{\mathrm{hys}} < 0$). Distortion of the shape of a hysteresis loop can have several causes. Tauxe *et al.* (1996) describe the variation in the shape of hysteresis loops due to mixtures of super-paramagnetic (SP) particles, where wasp-waisted loops can be the result of SD/SP magnetite with large SP particles, whereas SD/SP magnetite with small SP particles can result in potbellied loops. Generally, variation in the

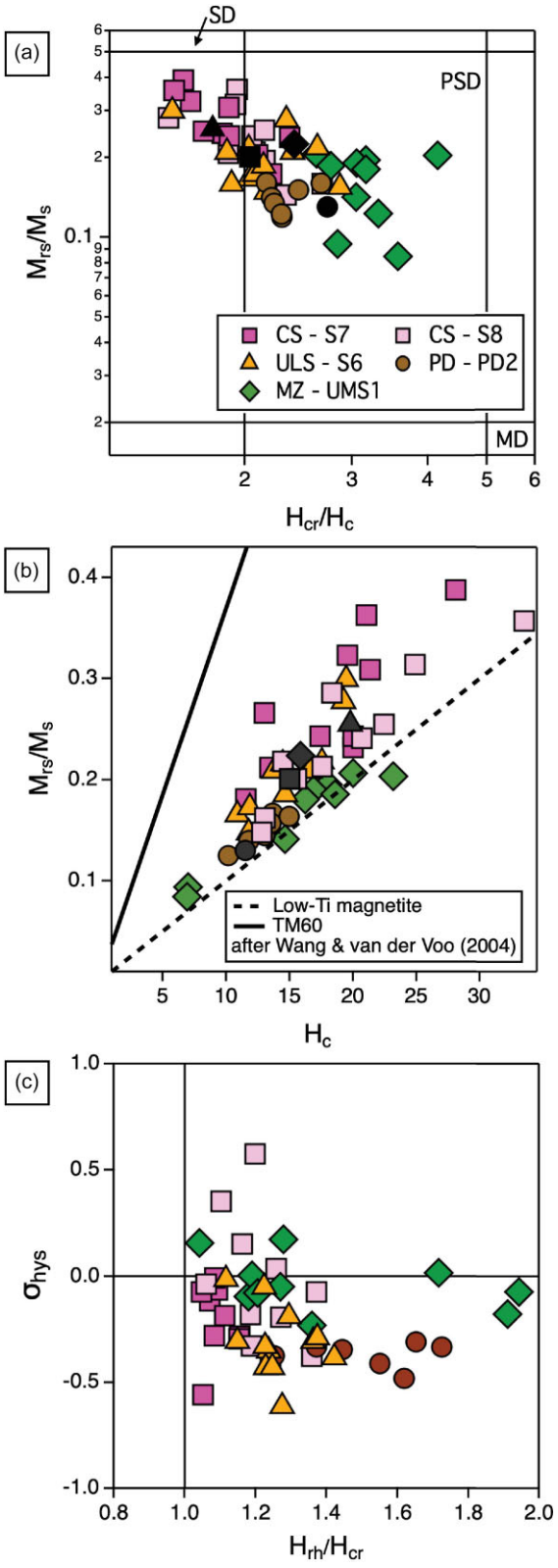


**Figure 4.** (a) Day plot after Day *et al.* (1977) with mixing lines and SD, PSD and MD regions from Dunlop (2002). (b) Squareness ($M_{rs}/M_s$) versus coercivity $H_c$. The formation means are indicated as black symbols. Lines for Low-Ti magnetite and TM60 from Wang & Van der Voo (2004) are shown for reference. (c) Shape parameter $\sigma_{hys}$ versus $H_{rh}/H_{cr}$ as described by Fabian (2003).

shape of hysteresis loops reflect a mixture of multiple coercivity components.

Based on Fig. 4(c), we infer that our samples do not contain SP grains because these would have a ratio $H_{rh}/H_{cr} < 1$ and $\sigma_{hys} > 0$ (Fabian 2003). However, the diagram suggests evidence of mixtures of multiple domain states, or magnetic carriers as discussed below. Most samples have negative $\sigma_{hys}$ values down to $-0.5$, with some exceptions from sites S8 and UMS1. These sites have positive $\sigma_{hys}$ values, indicating more wasp-waisted loops. The negative $\sigma_{hys}$ values suggest hysteresis loops with shapes ranging from ideal to more potbellied loops. The occurrence of these wasp-waisted loops suggests the samples contain a mixture of magnetic carriers with different coercivities. Aiming at investigating the origin of the shape of the hysteresis loops, IRM unmixing was used to distinguish multiple coercivity components, and FORC diagrams were used to distinguish different domain states.

### 4.4 IRM unmixing

Robertson & France (1994) demonstrated that the gradient of IRM acquisition curves could be modelled by multiple cumulative log-Gaussian (CLG) functions. This method was further developed by Stockhausen (1998), Kruiver *et al.* (2001) and Heslop *et al.* (2002). More recently, skewed generalized Gaussian (SGG) distributions have been argued to provide a more unbiased approximation (Egli 2003, 2004; Heslop *et al.* 2004; Maxbauer *et al.* 2016).

In this data set, the CLG and SGG methods provided the similar results, both in terms of peak locations and number of peaks required to fit the gradient data. The representative results of IRM unmixing using CLG functions are shown in Fig. 5. In most analyses, two dominant components were found, as well as an additional minor peak near one of the extremes of the total coercivity range. The coercivity distributions can be directly related to the magnetic mineralogy. From the complete data set, the lowest coercivity CLG distribution is centred at of measured samples have a minimum of 3.7 mT and the highest at 302.8 mT, and the median coercivity of remanence is 33.6 mT. The coercivity distribution of weakly magnetic CS dunite sample from site S7 (sample S7c), which contains Al-Cr-spinel with minor exsolution blebs as the dominant oxide, are fitted with two components that have mean coercivities close to each other with the main peak of the coercivity is centred at 30 mT. For the strongly magnetic CS samples (S8b, S8e), two distinct distributions were found (Figs 5b and c, respectively), both with a main component at ∼30 mT. Half of the samples show a pronounced high-coercivity component (Fig. 5c), which also commonly have positive $\sigma_{hys}$ values (Fig. 3c), indicating wasp-waisted hysteresis loops. This is the only site with a coercivity component higher than 200 mT. The ULS samples from site S6, which has magnetic carriers similar to the strongly magnetic CS site, does not show a high-coercivity component (Fig. 5d). The sample shows a low-coercivity component at ∼22 mT and a large peak at ∼34 m35 mT. The magnetic mineral phases in S8 and S6 are mainly Al-chromite with exsolved Cr-magnetite, and exsolved magnetite lamellae within clinopyroxene.

Sites PD2 and UMS1 have the same magnetic carriers, exsolved magnetite lamellae within clinopyroxene and discrete magnetite grains. In samples from PD2 site, there are dominant high- and subordinate lower-coercivity components at 41 mT and 16 mT. Some samples from site UMS1 have a high-coercivity component at 130–150 mT, (Fig. 5g), and two samples have a low-coercivity component at ∼17 mT (Fig. 5f). The UMS1 samples contain large

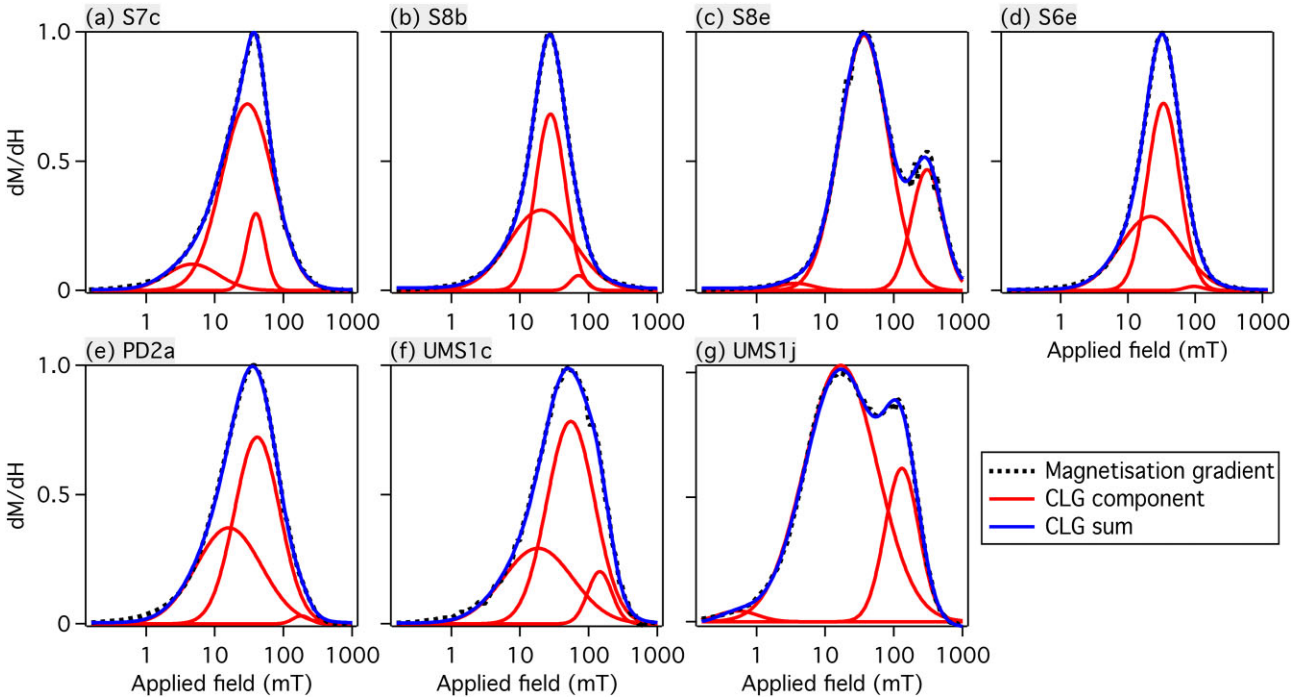


**Figure 5.** Representative IRM unmixing curves. Black dotted line is the processed measured IRM demagnetization curve, the red lines the calculated components, and the blue lines represent the fit from adding all components. These fits were obtained using CLG fitting functions; similar results were obtained using SGG functions.

discrete magnetite grains, (Fig. 10h), which may be the source of the low-coercivity component. Because these grains are found in discrete areas in the thin section, the rock chips used for the backfield curves may not contain this phase, which could explain why the low-coercivity peak is not present in all measurements. The largest coercivity distribution is shifted to a higher value in the UMS1 samples compared to the PD2 samples, at ∼55 mT (Fig. 5f). This peak may be generated by the exsolved magnetite lamellae in clinopyroxene, which are abundant in both sites. The exsolution lamellae in UMS1 are finer than those in PD2, which may explain the difference in coercivity.

### 4.5 FORC measurements

FORC measurements provide unique signatures for non-interacting and interacting single domain (SD), vortex and multidomain (MD) grains. In hysteresis loops the larger grains are commonly over-represented due to larger volumes. Here, FORC diagrams for five samples are shown (Fig. 6). A FORC diagram for the weakly magnetic dunite sample S7c, is shown in Fig. 6(a). This sample displays the dominant FORC signal around the origin with a lobe extending along the $H_u$-axis as well as the $H_c$-axis. The asymmetric lobe along the $H_c$-axis may be indicative of vortex state grains, whereas the contours extending parallel to the vertical axis indicates the presence of MD grains. FORC diagrams for dunite samples S8b and S8e (Figs 6b and c, respectively) show classic SD behaviour, with the negative region in the lower left-hand corner, as well as strongly interacting SD, spread off the $H_c$-axis. For sample S8e, there is a clear central ridge on the $H_c$-axis (dashed line) that extends to 500 mT. The signal beyond this value may be a processing artefact due to the high smoothing factor. This high-coercivity component is consistent with the IRM unmixing results, where this sample yields a high coercivity (of remanence) component centred at ∼300 mT. Sample S8b does not contain this high-coercivity component, or a high coercivity (of remanence) component in the unmixing curves. Both contain Cr-spinel with exsolved Cr-magnetite blebs.

Sample S6f (Fig. 6d), contains exsolved Cr-magnetite blebs from chrome spinel and exsolution lamellae of magnetite within clinopyroxene. FORC signal is parallel to the vertical axis and around the origin. The sample displays a central ridge along the $H_u = 0$ axis which extends to 200 mT, showing the presence SD grains, with the offset from the axis indicating these are interacting SD grains. The sample also displays the characteristic vortex state behaviour with closed contours, and contours diverging to the $H_u$-axis (Roberts *et al.* 2014).

Samples PD2b (Fig. 6e) and UMS1j (Fig. 6f), which both contain discrete magnetite and exsolved oxide lamellae within clinopyroxene, show a similar distribution to S6f. The dominant FORC signal concentrates around the origin and parallel to the vertical axis, indicating MD carriers. A lobe extends along and below the $H_u = 0$ axis which may indicate the presence of vortex state grains. Both samples show a central ridge along the $H_u = 0$ axis to approximately 200 mT for PD2b, and to 300 mT for UMS1j, respectively, characteristic for non-interacting SD grains. In summary, the FORC diagram of S7 is interpreted to provide the signature for the Al-Cr-spinel with exsolved Fe-rich blebs, because this is the only identified magnetic mineral in this sample. The FORC diagrams of the samples containing Al-chromite with exsolved Cr-magnetite blebs and exsolution lamellae from clinopyroxene both show the presence of MD, vortex state and non-interacting SD particles. The difference between these diagrams is the strong interacting SD component in S8. The only difference in mineralogy between S6, and S8, is the presence of a Cr-spinel in the latter, which contains fine exsolution, and is likely the source of the high-coercivity component. The dominant MD signal in PD2b and UMS1j can be attributed to the large discrete magnetite grains. This suggests that the vortex state and SD

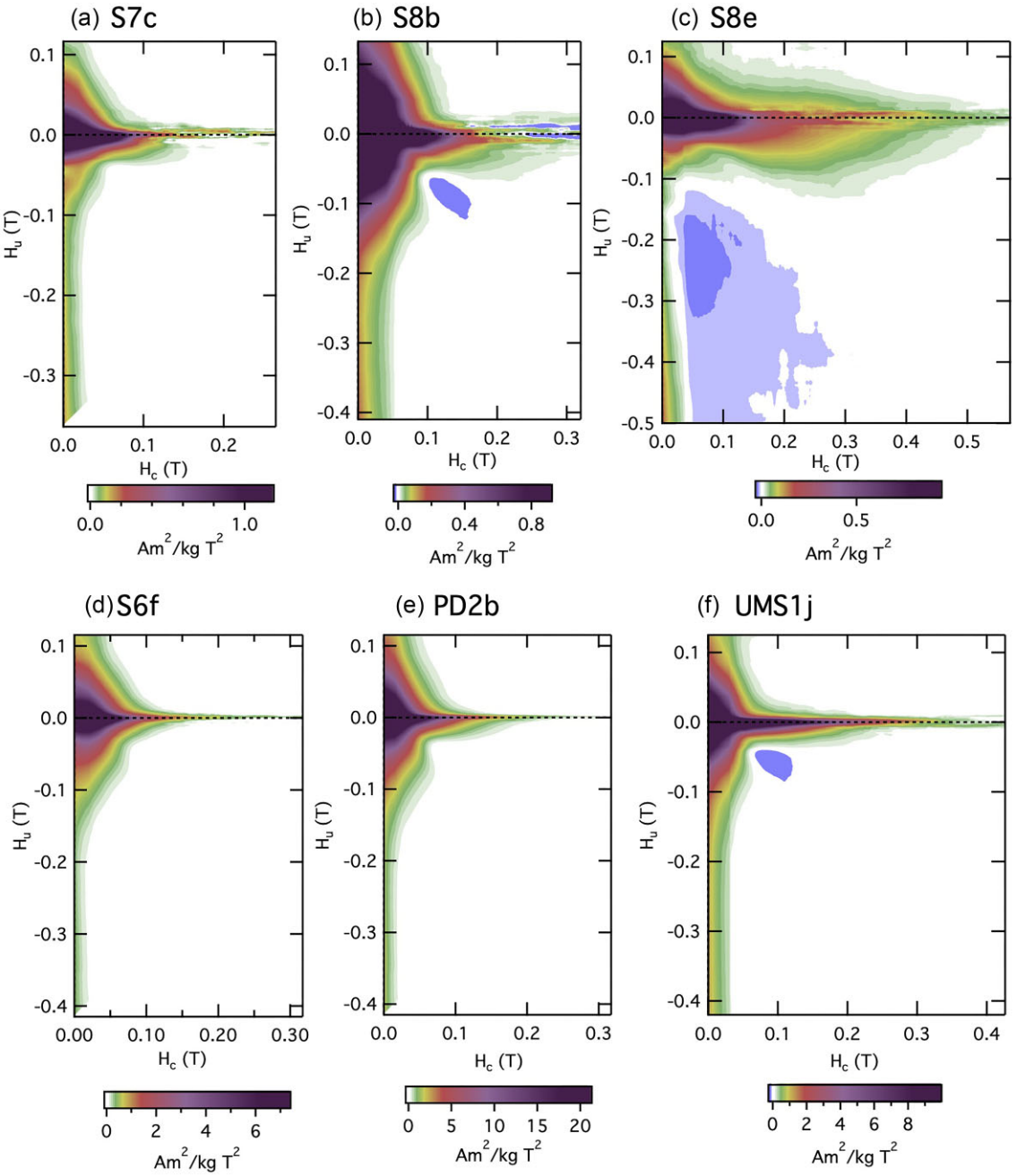


**Figure 6.** FORC diagrams of SMM samples, displaying characteristic signatures for SD, PSD and MD grains. Lambda for all graphs is 0.1 smoothing factors vary from 12 to 24.

particles represent the signature of the exsolved magnetite lamellae within clinopyroxene, which are also present in S6.

### 4.6 Thermomagnetic measurements

The temperature at which magnetic transitions occur can be diagnostic of mineral species and indicates potential deviation from stoichiometry. The Verwey transition in magnetite occurs at ∼125 K in stoichiometric samples (Walz 2002), but is highly sensitive to oxidation and composition. Deviations from stoichiometry initially depress the transition temperature, then, at higher degrees, suppress the transition entirely (Jackson & Moskowitz 2021, and references therein). Measurements of the Curie temperature ($T_c$) can also be diagnostic of the magnetic carriers and possible cation substitution. End-member magnetite has a Tc of 580 °C (853 K), but this transition temperature is progressively depressed by substitution.

The Verwey transition can be robustly examined using low-temperature remanence measurements. Field-cooled (FC) and zero-field-cooled (ZFC) remanence curves for four of the five samples are plotted in Fig. 7. Evaluation of the background -corrected derivative provides a precise estimation of the transition temperature that is used to infer chemical composition and stoichiometry of potentially distinct phases. The remanence loss at the Verwey transition can be different between the ZFC and FC curves, where multidomain populations have FC < ZFC below the Verwey transition temperature,

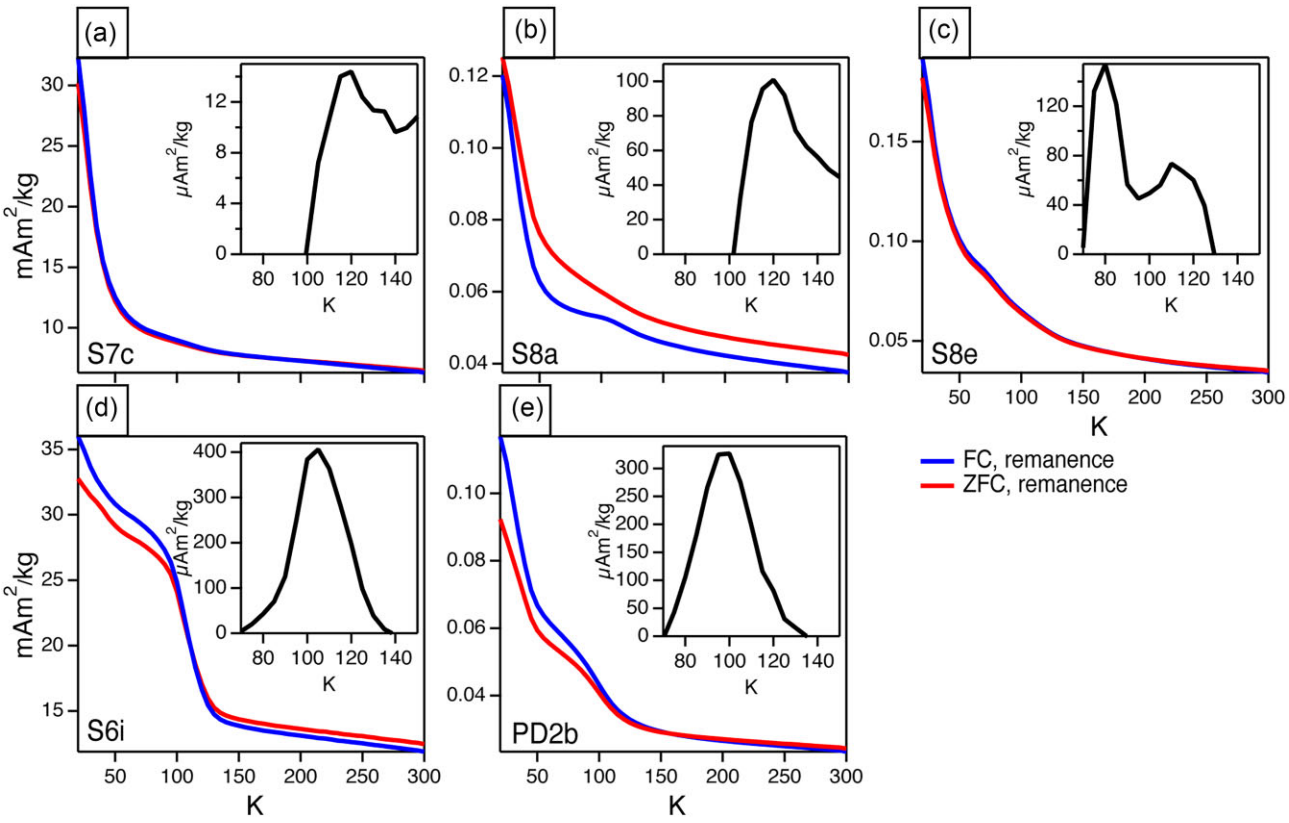


**Figure 7.** SIRM warming curves from 10 to 300 K for samples S7c, S8a; S8e, S6i and PD2b after cooling in a 2.5T field (Field-cooled, FC, blue) and in zero-field (zero-field cooled, ZFC, red). The insets show the background-corrected derivative ($-dM/dT$) of the FC curves.

and SD populations FC > ZFC (Smirnov 2009). SD grain populations have a larger remanence loss for FC than ZFC curves between 80 and 150 K (Moskowitz *et al.* 1993), whereas larger (MD) grains have similar fractional remanence loss in ZFC and FC curves.

The ZFC and FC measurements of weakly magnetic CS sample S7c (Fig. 7a) are virtually identical and the change in magnetization at the Verwey transition (-dM/dT) is an order of magnitude smaller than the other samples. This transition occurs at ∼120 K, implying near-stoichiometry.

The strongly magnetic CS sample S8a (Fig. 7b) has a small kink at the Verwey transition in the FC warming curve, which is not visible in the ZFC curve. In this sample ZFC > FC, whereas in the other CSsample, S8e, the curves overlap (Fig. 7c). On the graph for S8e very small transitions are visible at 80 and 110 K. In sample PD2b a Verwey transition is visible at ∼100 K, and a lower temperature transition at ∼50 K is visible in this sample as well as in S8e and S6i. The depressed Verwey-transition temperature of 100 K suggests with some degree of cation substitution or non-stoichiometry in the magnetite lamellae in the pyroxene. The 50 K transition temperature in all measurements is likely due to the onset of long-range ordering in ilmenite, with a temperature of 57 K for pure ilmenite, and lower temperatures due to substitution, commonly of Fe, Mn or Mg (McEnroe *et al.* 2007; Burton *et al.* 2008).

SIRM warming curves of ULS sample S6i (Fig. 7d) show a Verwey transition at 105 K, again indicating the presence of slightly non-stoichiometric magnetite, and the FC curve is higher than the ZFC curve at low temperatures.

Samples S8a, S8e and S6i, which share the same magnetic carriers, display differing behaviour. The ZFC-FC curves imply the presence of MD grains in S8a, and SD grains in S6i. The Verwey transition temperature in S6i indicates the presence of cation-substituted magnetite, which may be attributed to the exsolution lamellae of magnetite within clinopyroxene, which are more abundant in S6. The FORC diagrams (Fig. 6) for these samples show the presence of MD, SD and vortex-state grains in these samples. The low-$T$ curves for PD2 indicate the presence of SD grains, with FC > ZFC below the Verwey transition, also consistent with the FORC diagram.

Thermomagnetic measurements of mass-specific susceptibility were measured on a Kappabridge (Figs 8a–e), from −195 to +700 °C. Measurements were made in argon to avoid alteration by oxidation, yet all but one show a minor increase in susceptibility from the heating to the cooling curve, suggesting some chemical, or structural change at high temperature. High-temperature VSM measurements on sister samples were also acquired. These measurements provide $M_s$, $M_{rs}$ (Figs 8f–j) and high-field susceptibility $\chi_{HF}$ (0.7–1 T; Figs 8k–o) from room temperature to 700 °C (Fabian *et al.* 2013). The $T_c$ was obtained from the $M_s$ versus temperature curves using the derivative method, by calculating the point of steepest descent, and the blocking temperature was estimated using the same method on the $M_{rs}$ curves. However, the blocking temperatures are approximate because the unblocking process occurs over a temperature range that depends on the distribution of grain sizes and shapes of the magnetic carriers in the sample. Samples from site S7 show no low-temperature transition in either of the low-$T$ measurements. The measurements for S7c are consistent between the Kappabridge low-temperature susceptibility and the SIRM warming curves, displaying no Verwey transition, implying that the exsolved Fe- phase from the Al-Cr-spinel is non-stoichiometric, or contains

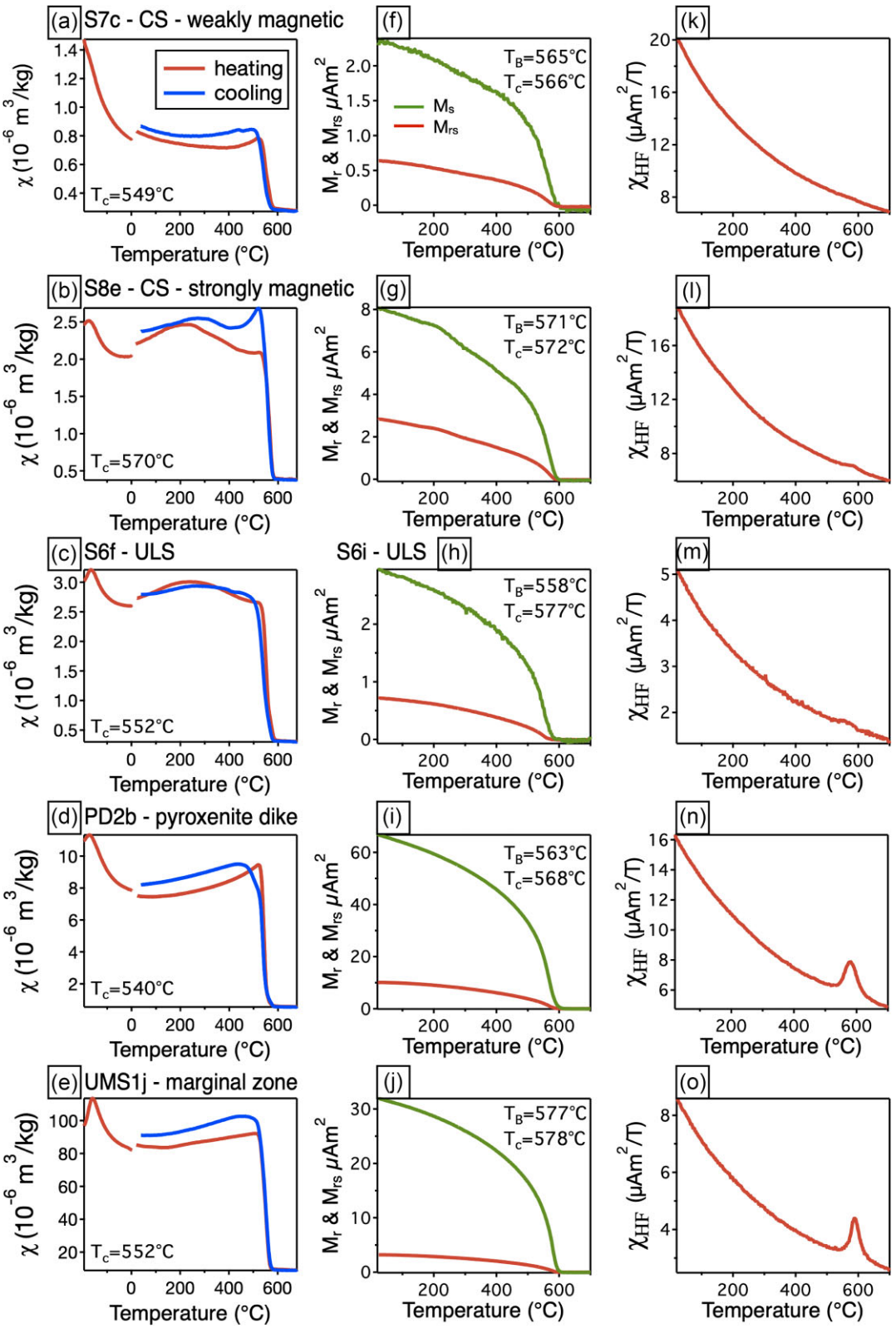


**Figure 8.** (a–e) $\chi$–$T$ curves of the selected samples with heating curves in red, cooling in blue. (f–j) High-temperature curves: $M_{rs}$ (red) and $M_s$ (green) versus temperature. (k–o) High-field susceptibility versus temperature.

a degree of cation-substitution. Both samples from site S8 (Figs 8b and c), and to a lesser extent, those from site S6 (Fig. 8d, show a concave-down shape in the high-temperature curves. The susceptibility in these samples increases up to ∼200 °C, followed by a slow decrease until ∼540 °C, above which a rapid decrease follows. Site S6 samples yield lower $T_c$'s than those of S8. The Curie temperatures combined with the low-temperature transition indicate the presence of near-end-member magnetite in these samples. There is

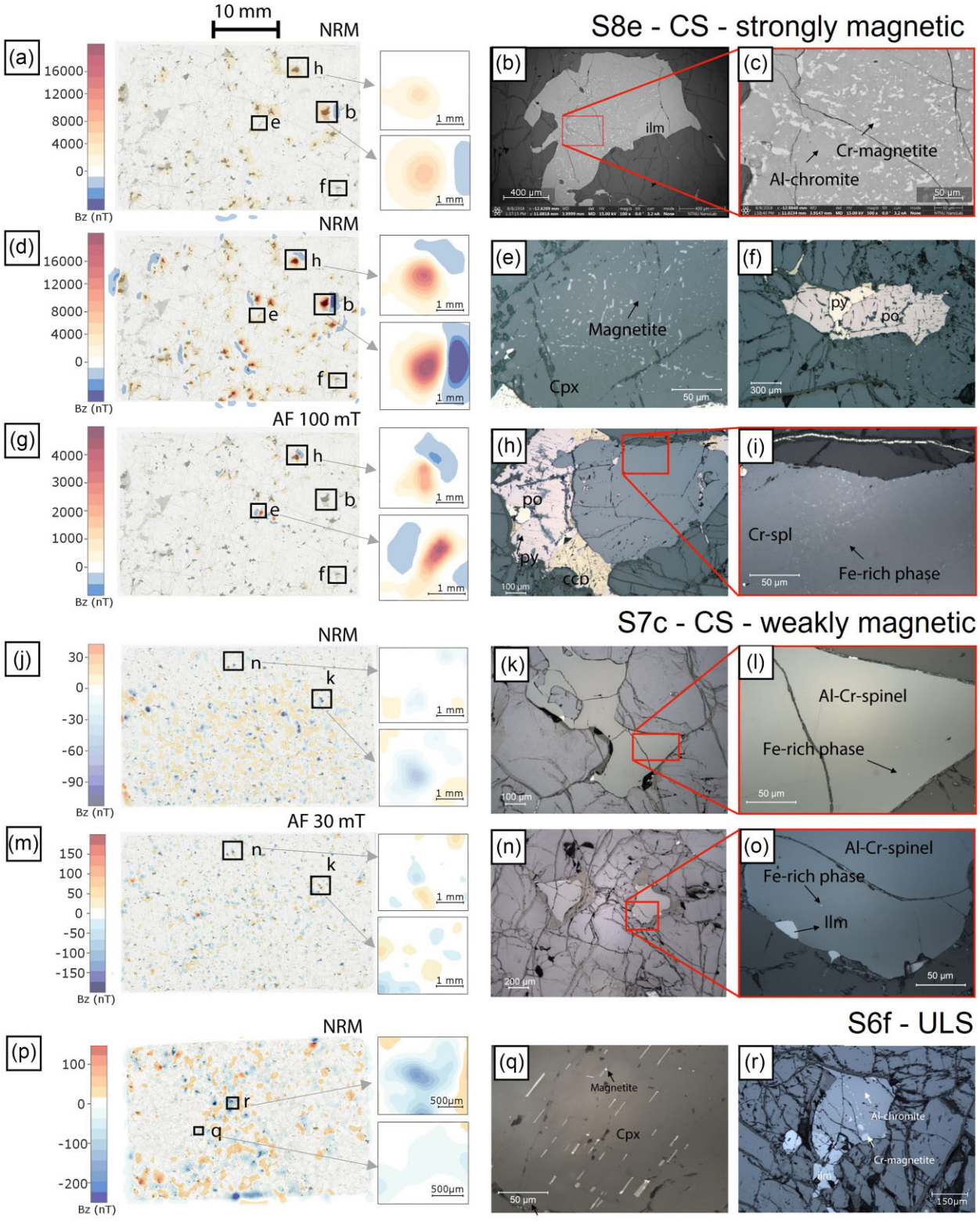


**Figure 9.** Overlay of the magnetic anomaly maps on the optical scans of samples S7c, S8e and S6f, with colour scale bar in nT. NRM magnetic scans with a SQUID microscope were made before (a, j, p) and after partial demagnetization (g, m). Additional NRM scans were obtained using the MTJ microscope on sample S8e using the MTJ microscope (d): an NRM scan and a scan after partial demagnetization. Black boxes indicate the locations of the detailed magnetic anomaly maps and micrographs with the same letter. For some higher magnification images are shown using the red boxes. All images expect except (b) and (c), which are BSE images, are reflected light images. ilm: ilmenite, cr-spl: chrome-spinel, cpx: clinopyroxene, py: pyrite, po; pyrrhotite, ccp: chalcopyrite.

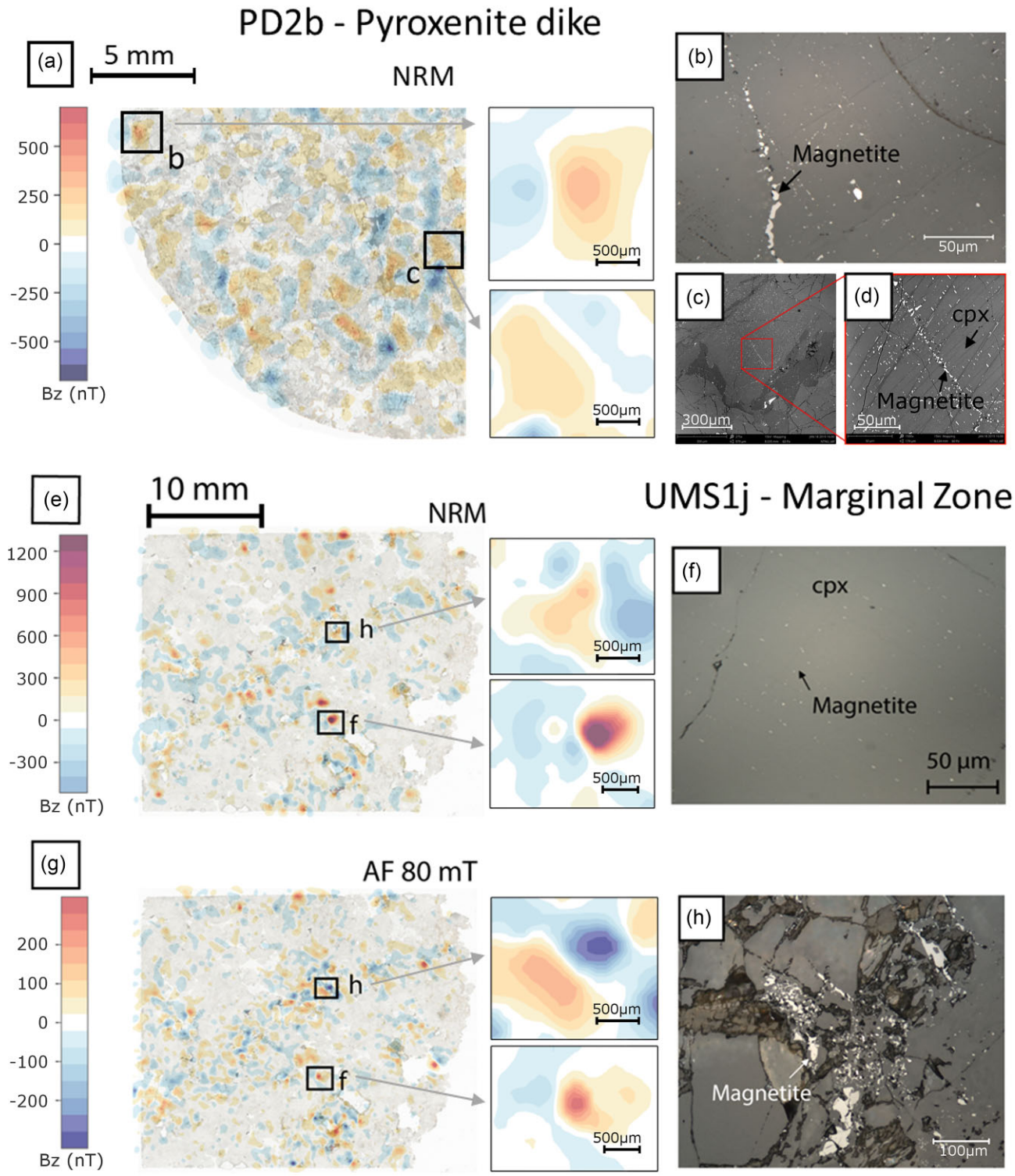


**Figure 10.** Overlay of the magnetic anomaly map on the optical scan for PD2b (a) and for UMS1J before (e) and after partial AF demagnetization (g). On the left of the magnetic scan is the respective colour scale bar in nT. Black boxes indicate the locations of the adjacent micrographs. Photomicrographs are reflected light images (b, f, h) and BSE (c, d).

a large difference between $T_B$ and $T_c$ in the sample of S6, 558 and 577 °C, respectively, potentially indicating the presence of small single-domain particles that unblock at temperatures measurably below the $T_c$. This inference is consistent with the observation of a central ridge in the FORC diagram from this sample (Fig. 6d). All samples of S8 and S6 show a Landau peak on the high-field susceptibility curve (Fig. 8l). This peak occurs at temperatures slightly above the $T_c$ and is indicative of ferrimagnetic ordering (Fabian 2003).

Sample PD2 shows a low-temperature transition, which is not sharp and occurs at a lower temperature than literature values for Verwey transition. The depression of this transition temperature by

∼15 °C suggests that the magnetite has a small degree of non-stoichiometry, either in the form of oxidation or cation substitution. The degree of this non-stoichiometry varies, yielding the range of transition temperatures that prevent a single abrupt change in magnetic properties. In samples UMS1f and UMS1j a clear Verwey transition is present, and the samples have a $T_c$ of 543 and 552 °C from susceptibility. MZ sample UMS1j has the highest $T_B$ and $T_c$ determined from the VSM measurements and these are close at 577 and 578 °C.

### 4.7 Scanning magnetic microscopy

SMM provides high-resolution mapping of magnetic fields above a planar surface of a rock sample, or a thin section. In field-free conditions, the technique measures the vertical component of the magnetic field originating from the sample's remanent magnetization. Magnetic mapping of samples aid in resolving the ferromagnetic carriers at small scales (Egli & Heller 2000; Weiss *et al.* 2007, 2019, 2021, 2022; Hankard *et al.* 2009; Oda *et al.* 2011; Lima & Weiss 2016; de Groot *et al.* 2018; Pastore *et al*. 2018a).

Here, the magnetic scans were acquired on thin sections and the remanent carriers were mapped and correlated to the NRM. The magnetic field intensity range varies in proportion to the magnetic properties of the mineral grains. The magnetic scans of samples with high susceptibility and NRM show higher field intensities. Aligned overlay images of optical and magnetic scans of the thin sections commonly show a correlation of the mapped magnetic anomalies with the opaque mineralogy (Figs 9 and 10).

Thin sections S8e, S7c and UMS1j were scanned both in their NRM state and later alternating field (AF) demagnetization at fields of 100, 30 and 80 mT, respectively. The field at which the samples were demagnetized was determined by the results of IRM unmixing spectra shown in Fig. 5. The coercivity spectra of these samples show two components (Fig. 5) and an AF field intermediate to the two peaks was chosen to observe the effect of preferentially demagnetising the low-coercivity phase.

#### *4.7.1 CS dunite samples S8e and S7c*

Thin section S8e was scanned with both the magnetic tunnel junction (MTJ; Fig. 9d) and the SQUID instruments (Figs 9a and g). The two instruments used different sensor elevations due to the strong magnetic signal of the sample. The sample was measured at operating height of 150 μm with the MTJ scanner, however, the sample was too magnetic to be measured at this height with the SQUID instrument, therefore a glass plate of 0.8 mm thick was inserted. The magnetic field intensity measured with the MTJ instrument ranges from −7473 to 23 161 nT (Fig. 9d) while that measured with the SQUID instrument ranges from −1877 to 7218 nT (Fig. 9a), which is comparable with the range for an upward continuation of the MTJ scan data to the same height. The magnetic field of the demagnetized thin section, measured with the SQUID at a height of 295 μm, has a range of −790 to 5479 nT (Fig. 9g). Site S8 has a mean NRM of 1.1 A m$^{-1}$, an order of magnitude higher than the mean NRM of site CS S7 of 0.17 A m$^{-1}$.

The magnetic scans show multiple magnetic anomalies, commonly dipolar, indicating magnetizations approximately in the plane of the sample and with different azimuths. The anomalies are located over both large and small opaque grains (Figs 9b–c, e–f and h–i), with those of highest amplitude are associated with the largest opaque grains. The scan after AF demagnetization (Fig. 9g) shows an overall decrease in field intensity, however there are two areas (e and h, discussed below) that retain a substantial magnetization after AF demagnetization. Note the colour scales are different on the two scans. This decrease in magnetization is the result of removing softer components of the magnetization by demagnetising the sample in an alternating field. The resulting scans record the remaining magnetization in the phases with coercivities >100 mT.

Most large opaque grains are Al-chromite grains with associated ilmenite grains (Fig. 9b). The Al-chromite contains exsolution blebs of Cr-magnetite (Fig. 9c). The Cr-magnetite exsolution has a range of sizes, from submicron up to 40 μm in diameter. The opaque grains that are sulphides (chalcopyrite, pyrite, pyrrhotite; Fig. 9f) have no clear magnetic anomaly associated with them in the magnetic scans before, or after, demagnetization of the thin section (Figs 9a, d and g). In one case, the sulphides are associated with a large Cr-spinel grain of unidentified composition that contains very fine exsolution microstructures (Fig. 9h). This grain retains a magnetization after AF treatment (Fig. 9g). Another area in which magnetic anomalies remain after AF demagnetization is over a clinopyroxene grain with fine magnetite exsolution lamellae (Fig. 9e). The phases that retain their magnetization after AF demagnetization are the likely carriers of the high-coercivity SD signal observed in the FORC diagram, and in the IRM unmixing diagram. Dunite sample S7c has a site mean NRM of 0.17 A m$^{-1}$, which is an order of magnitude weaker than that of site S8 (1.1 A m$^{-1}$). The magnetic scan for sample S7c (Fig. 9j) has weaker field intensities than that for sample S8e (Figs 9a and d). For S7c the magnetic field ranges from −216 to 94 nT for the scan acquired before AF demagnetising the thin section. The magnetic field ranges from −220 to 258 nT for the scan made after AF demagnetization at 30 mT. The magnetic anomalies in Figs 9(j) and (m) commonly exhibit negative field values, which implies the magnetization is perpendicular to the scanned surface and magnetized into the plane of the sample. A few dipolar anomalies that correlate with opaque grains are observed at the edge of the thin section. In the magnetic scan acquired after AF demagnetization, there are more dipolar anomalies, indicating the magnetization is then in the plane of the thin section. This may be due to removal of a softer out-of-plane component that masked the in-plane magnetization. Figs 9(k)–(l) and (n)–(o) are reflected-light images of grains that are correlated to the magnetic anomalies. Fig. 9(k) shows the source of one strong anomaly in the sample, an Al-Cr-spinel grain with fine-grained exsolution blebs, which are visible in the higher magnification image (Fig. 9l). Fig. 9(n) shows the source of one of the weaker anomalies in the sample. The grain is an Al-Cr-spinel with ilmenite at the edges. Only one small exsolution bleb is visible in this grain.

#### *4.7.3 Wehrlite sample S6F*

The field intensity for the magnetic scan of thin section S6f ranges from −370 to 241 nT (Fig. 9p). The mean NRM for site S6 is 0.69 A m$^{-1}$. Most strong anomalies in the thin section correlate clearly with the larger opaque grains, while more diffuse signals are visible over areas with no visible discrete opaque mineralogy. The silicate phases are olivine and clinopyroxene. The sample has two regions, which are more clinopyroxene-rich (left of box 'q' and lower right-hand corner of the thin section), over which no anomalies are seen. The observed anomalies are randomly oriented dipolar anomalies

in the magnetic scan. The anomalies with higher amplitude are associated with large opaque grains consisting of Al-chromite with exsolved Cr-magnetite blebs (Fig. 9r). The regions of the thin section dominated by pyroxene show fewer anomalies than areas with more olivine and co-existing large opaque grains. However, some diffuse anomalies are observed over clinopyroxenes that contain minor lamellae of magnetite, and more abundant ilmenite exsolution lamellae (Fig. 9q).

#### *4.7.4 Pyroxenite dyke PD2b*

The magnetic field intensity for the PD2b scan (Fig. 10a) ranges from −1503 915 nT. The mean site NRM is 8.4 A $m^{-1}$. The magnetic scan shows randomly oriented anomalies. In Fig. 10(a), the regions for which the mineral sources are shown (b, c) represent the typical anomaly in the sample, rather than the outstanding anomalies. These anomalies correlate with the presence of magnetite exsolution lamellae in clinopyroxene (Fig. 10c) and small discrete magnetite grains (Fig. 10b), at grain boundaries, and dispersed in the matrix. Areas where anomalies are not observed are either olivine grains (colourless) or clinopyroxene grains. The large opaque grains not associated with anomalies are ilmenite grains and these do not contain exsolution lamellae.

#### *4.7.5 Marginal zone pyroxenite sample UMS1j*

The magnetic field intensity of sample UMS1j ranges from −992 to 1854 nT for the scan acquired before demagnetising the sample (Fig. 10e). For the scan acquired after AF demagnetization at 80 mT the range is from −495 to 692 nT (Fig. 10g). The site mean NRM is 2.64 A $m^{-1}$. The amplitudes of the magnetic anomalies are comparable to those from PD2b. The observed anomalies have varying orientations and are mostly located over large clinopyroxene grains which contain magnetite exsolution lamellae (Fig. 10f) and over discrete magnetite grains (Fig. 10h). Some opaque grains in this sample do not yield anomalies, and are non-magnetic sulphides, or ilmenite. After AF demagnetization the magnetic anomalies show a reduction in amplitude with the highest amplitude decrease by 60–80 per cent after demagnetization.

## 5 DISCUSSION

### 5.1 Magnetic phases in the RUC

The pristine ultramafic samples contain varying amounts of Al-chromite with exsolved Cr-magnetite, Al-Cr- and Cr-spinel with exsolution blebs of a more Fe-rich phase, of near end-member magnetite, clinopyroxene with exsolved magnetite lamellae and discrete magnetite. All samples contain at least two of these carriers, except for S7, in which only Al-Cr-spinel with Fe-rich exsolution blebs are observed. The ilmenite, where observed, does not contain any exsolution, and here is considered to be paramagnetic.

#### *5.1.1 The CS and ULS*

The CS and ULS are dominated by olivine, and varying amounts of pyroxene. The CS dunites are olivine with up to 10 per cent clinopyroxene (Grant *et al.* 2016). The ULS consists of dunite and wehrlite, with up to 46 per cent clinopyroxene (Grant et al. 2020, and references therein). Two pristine CS sites were selected from the 14 CS sites, based on magnetic properties. Site S7 has the lowest NRM and susceptibility values of the CS formation, while site S8 is among those sites with the highest values (Fig. 3). Site S6 was selected as a representative site for the ULS rocks. All ULS sites are dominated by olivine and Cr-spinel, though in S6, clinopyroxene is also abundant. In S7 the spinel is an Al-Cr-spinel with a fine-grained Fe-rich exsolution phase, which is the only magnetic carrier in these samples (Figs 9k, n). The dominant spinel in S8 and S6 is Al-chromite with exsolution blebs of Cr-magnetite (Fig. 9b), and in S8 a Cr-spinel with an exsolved Fe-rich phase is also present (Fig. 9h). The Cr-magnetite exsolved from Al-chromite ranges is size from submicron blebs to several tens of microns. The exsolved phase from the unidentified Cr-spinel is much finer, commonly submicron in size. Clinopyroxenes in S6, and to a lesser extent in S8, contain exsolution lamellae of magnetite, Cr-magnetite and ilmenite.

In the weakly magnetic CS sample, S7, the thermomagnetic measurements show a $T_c$ of 549 °C and no low-temperature transition (Figs 8a, f and k), indicating the magnetic carrier is magnetite with some degree of cation substitution or non-stoichiometry. The $T_c$'s in S7 are consistently low and show a sharp decrease in susceptibility and magnetization near the $T_c$, indicating a relatively narrow range in compositions. By contrast, CS sample S8 and ULS sample S6 display a broad range in $T_c$'s (Figs 8b–c; g–h and l–m). Site S6 and S8 contain Al-chromite with Cr-magnetite exsolution as the dominant magnetic carrier, and the high-T susceptibility and high-T VSM curves for most samples containing this phase display a more gradual decrease in susceptibility and magnetization in the concave down curves near the $T_c$, with the susceptibility or magnetization decreasing above 250 °C, and have an average $T_c$ of 554 °C. The gradual decrease in susceptibility is interpreted as evidence for a range in Cr-magnetite compositions in the exsolution blebs from Al-chromite, which range in size from submicron to ∼40 μm. The presence of a Verwey transition in some samples from sites S8 and S6 implies the presence of (near-) end-member magnetite. This signal could be from Fe-richer exsolution blebs within the Al-chromite, and/or the magnetite lamellae in clinopyroxene. The FORC diagrams of ULS sample S6f and CS sample S8e, show a range in domain states, from interacting and non-interacting SD, vortex state to MD. The broad range in grain sizes of the exsolved Cr-magnetite from Al-chromite could account for the different domain states interpreted in the FORC diagram.

Comparing the volume per cent magnetite in the CS and ULS samples we find the lowest percentage in the CS dunite samples, which mainly contain exsolved Al-Cr-spinel grains with minor amounts of exsolution. The S7 site samples have a mean volume per cent of magnetite of 0.033 per cent calculated from susceptibility, and 0.028 per cent calculated from the saturation magnetization. The samples with Al-chromite have an estimated mean volume per cent magnetite of 0.11–0.26 per cent based on susceptibility values, and 0.10–0.23 per cent magnetite when calculated from $M_s$ values.

Like the NRM and susceptibility measurements, the mean $M_{rs}$ and $M_s$ values in site S8 are an order of magnitude larger than in site S7 (Table 1). The results from ULS site S6 fall between those of CS sites S7 and S8, mirroring their NRM and susceptibility values. By contrast, the $H_c$ values of S7 and S8 are similar, and higher than those found in S6. The IRM unmixing results (Figs 5a–c) from S7 and S8 show a main peak location at ∼35 mT, although some S8 specimens also exhibit a high-coercivity component (>100 mT). The backfield unmixing of S6 (Fig. 5d) yields main peak location at 34 mT. The FORC diagrams for S8 (Figs 6b and c) and S6 (Fig. 6d) show MD, vortex state and SD signatures. In addition, S8 contains a central ridge extending out to 500 mT. S7 contains mainly MD and vortex state signatures.

The samples from site S8 that contain the high-coercivity component in the IRM unmixing also display wasp-waisted hysteresis loops (Fig. 4c) and show a high-coercivity SD component in the FORC diagram (Fig. 5e). The extension of the FORC signal to 500 mT would seem to exceed the maximum coercivity of uniaxial SD magnetite particles of 240 kA $m^{-1}$ or 300 mT (Dunlop & Özdemir 1997; Church et al 2016). The high coercivity components found in S8e may indicate the influence from an additional mechanism such as the presence of internal stress in very small exsolved particles.

#### *5.1.2 Mineral and petrological origins of variability in the CS*

The CS lacks the modal layering found in ULS or LLS formations, though variation in olivine composition with stratigraphic height is reported (Grant *et al.* 2016, 2020). In our samples we observed a distinct variation in the magnetic properties between sites S7 and S8, which are likely due to changes in the modal mineralogy. The bulk magnetic measurements show site S8 has a higher concentration of magnetic minerals, and a larger range in domain states compared to site S7.

The olivine grains in S8 are larger (up to 1 cm) than in S7 (up to 400 μm). A similar distinction is observed in the spinel phases with the largest grains present in S8 and the smallest in S7. The composition of the spinel is different between these sites: Al-chromite is the dominant host spinel in S8, and Al-Cr-spinel is the dominant host spinel in S7. Both host spinels are chrome-rich, and the main difference is Fe content. It is possible that $Fe^{2+/3+}$ charge ordering between the lamellae and host may influence the total magnetization as found in lamellae formed in the ilmenite hematite system (Robinson *et al.* 2006) and proposed for magnetite-ilmenite (Robinson *et al.* 2016).

The calculated volume per cent magnetite was estimated from the susceptibility (Balsley & Buddington 1958) and Ms values. Using these two methods a median magnetite volume percentage of 0.03 per cent was obtained for S7 from both methods, and in S8e 0.22 per cent from susceptibility and 0.16 per cent from $M_s$ These values may be a slight underestimate of the total volume because the magnetic carriers in these samples are not end-member magnetite. The difference in volume per cent magnetite between S7 and S8 is nearly an order of magnitude, in good agreement with the magnetic properties.

Energy-dispersive X-ray spectroscopy (EDS) measurements reveal clear variations in the CS spinels (Fig. 2 and Pastore *et al.* 2016). In S8 the host is an Al-chromite, and a Cr-magnetite as the Fe-rich exsolved phase. The average composition of the host spinel phase in S7 is richer in aluminium and poorer in iron than the chromite in S8 (Fig. 2) and the exsolved phase in S7 was too small for EDS analyses, but here is interpreted as near end-member magnetite based on the thermomagnetic measurements Pastore *et al.* (2018b) determined compositional data on spinels in a CS dunite sample CS4 showing a strong partitioning of iron into micron to submicron exsolved blebs. The composition of these blebs in CS4 is similar to those in S8, while the host spinel composition is Al-richer and Fe-poorer than the averaged S8 host composition. The compositional variations of spinel reported here and by Pastore *et al.* (2018b) and the variations in olivine composition as reported by Grant *et al.* 2016 for the CS dunites may be the result of the cryptic layering, possibly reflecting two different magmas. Another possible explanation for the variations in spinel composition may be related to fractional crystallization and melt replenishment (Grant *et al.* 2016).

#### *5.1.3 Pyroxenite dykes and the marginal zone*

The pyroxenite dykes, and marginal zone formations have different origins, but contain similar magnetic carriers. Samples from both formations (PD2 and UMS1) contain clinopyroxene grains with exsolved ilmenite and magnetite lamellae, in addition to discrete magnetite grains. In contrast to the CS and ULS samples, these samples do not contain Al-chromite or Al-Cr-spinel.

The thermomagnetic measurements of PD2 and UMS1 show similar behaviour. The occurrence of a Verwey transition in the low-temperature measurements of PD2 indicates the presence of (near-)end-member magnetite (Fig. 8d). However, the $T_c$ of 540–568 °C suggests that some magnetite has some cation substitution (Figs 8i and n). Likewise, the low-temperature measurements of UMS1 display a Verwey transition (Fig. 8e), and the Curie temperatures are 552–578 °C (Figs 8j and o), which suggests the presence of a near-end-member magnetite with a small degree of cation-substitution.

While site PD2 yields the highest magnetization, the site yields the lowest median coercivity values (Table 1). The median $M_{rs}/M_s$ ratio is 0.14, while the $H_{cr}/H_c$ ratio is high with a value of 2.29. The dominant FORC signal indicates MD and vortex state particles, and non-interacting SD particles (Fig. 6e). Backfield unmixing yields a median peak location at 22.5 mT (Fig. 7e). No high-coercivity components are observed in these samples. The presence of large magnetite grains may explain these properties.

The samples of UMS1 have similar $M_{rs}/M_s$ values to PD2 and have the highest ratio $H_{cr}/H_c$ of all samples reported here, and plot near the MD region on a Day plot (figs 4a and 8 in ter Maat *et al.* 2019) and closest to the origin in the squareness-coercivity diagram (Fig. 4b). The shape of the hysteresis loop is close to the ideal hysteresis shape, whereas the shape of hysteresis loop for PD2 is closer to potbellied. The variation in $H_{rh}/H_{cr}$ ratio can be attributed to the amount of MD material in the sample (Fig. 4c). The FORC distribution is similar to that of PD2, with a dominant MD signal, and evidence of vortex state and SD particles, with a clear non-interacting central ridge up to 300 mT (Fig. 6f). The main difference between the PD2 and UMS1 samples is the presence of a high-coercivity component up to 200 mT in the IRM unmixing analysis of UMS1 data (Figs 5f and g). The unmixing and central ridge properties likely reflect the contribution of smaller magnetite lamellae in the clinopyroxene (Fig. 10f).

### 5.2 Using SMM to correlate signatures to carriers

Pastore *et al.* 2018b, 2021, 2022) and Lee *et al.* 2023 using SMM data made magnetic inversions on individual grains, and also inverted data from entire thin sections, and both reported a good correlation between the modelled individual grains and bulk sample's magnetization directions. Here we used SMM to correlate the mapped magnetic anomalies by SMM to their mineral sources, and further to assess the influence of microstructure on their magnetization.

In the CS and ULS formations we attribute the stable source of magnetization to the fine exsolution of Cr-magnetite, and the Al-chromite grains. The exsolved phase ranges in size from submicron to >40 μm. In addition, in CS site S8 an unidentified Cr-spinel in assemblage with pyrrhotite, pyrite and chalcopyrite, contains a submicron exsolution texture. Here monoclinic pyrrhotite can be excluded as a magnetic carrier because of the lack of anomalies associated with sulphides, and the absence of a magnetic transition at 320 °C. To verify if the fine exsolved microstructures in the

spinels and clinopyroxenes are the stable source of the magnetization we used SMM prior to, and after, AF demagnetising of the thin sections. This allowed for the identification of which phases were associated with remanent magnetic anomalies, before, and after demagnetization.

In the ultramafic formations, CS and ULS, the magnetic anomalies are mainly observed associated with the opaque grains. Generally, the opaque grains where no anomalies are seen are sulphide phases. In S6f the anomalies occur over Al-chromite grains with exsolved Cr-magnetite, and over clinopyroxene with exsolution lamellae of magnetite and ilmenite. In sample S8 most anomalies are over Al-chromite grains, which have abundant Cr-magnetite exsolution. One large spinel grain with submicron size exsolution of unidentified composition is found in association with chalcopyrite–pyrite–pyrrhotite.. We infer this exsolution is an Fe-rich phase because of the distinct magnetic anomaly in the magnetic scans. This phase is shown to be magnetically stable with only a minor reduction in magnetization even after the application of an AF field of 100 mT. We infer that this exsolution in the spinel grains are the source of the high-coercivity components in the FORC diagram and the IRM unmixing curves.

In these ultramafic samples, olivine grains were not associated with any magnetic anomalies but pyroxene grains with magnetite exsolution lamellae were correlated with the magnetic anomalies. In the S6 thin section, the exsolution lamellae in the clinopyroxene grains were commonly paramagnetic ilmenite. However, there was rare magnetite exsolution lamellae, however it was volumetrically minor and may not produce a measurable anomaly.

The exsolution lamellae in clinopyroxene range in size in the ultramafic different formations, with the finest exsolution blades present in the MZ rocks. These blades may represent the source of the SD signal observed in the FORC diagrams of all samples containing clinopyroxene. The discrete magnetite grains in the PD and MZ samples have a large size range from 1 to 50 μm. These grains are the likely source of the vortex state to MD signal found in the FORC diagrams.

The rocks assessed here acquired their magnetization cooling through the solvus temperature of the Cr-magnetite and Al-Cr spinel at a temperature slightly below 600 °C. The effect of pressure on the Curie temperature may enhance the Curie temperature at lower crustal levels up to 20 °C (Schult 1970; Gilder & Le Goff 2008). In addition, the effects of pressure on the consult points in the different oxide systems, which would have consequences on the stability of two (or more) phase in these systems is not adequately understood, nor are the effects of non-equilibrium reactions in the oxides (McEnroe *et al.* 2004a, 2009, 2018).

## 6 CONCLUSION

A combination of petrophysical, rock magnetic and SMM measurements were made on a suite of ultramafic (dunite–wehrlite) samples from the Reinfjord Ultramafic Complex. The primary magnetic carriers were identified *in situ* using SMM, and are linked to specific rock magnetic properties, including coercivity unmixing and FORC diagrams. The composition of the magnetic carriers is inferred from thermomagnetic measurements. SMM is used to confirm the mineral sources and the stability of the magnetization.

The dominant magnetic mineralogy in the pristine ultramafic samples, are Fe-rich exsolution blebs from Cr-spinel, and exsolution lamellae of magnetite in clinopyroxene. These are considered part of the primary igneous assemblage. The range of Curie temperatures in these samples is from 535 to 550 °C, excluding any pressure effects. The calculated mean total magnetization irrespective of direction for the ultramafic formations CS, ULS and LLS with densities above 3.2 g cm$^{-3}$, is 1.4 A m$^{-1}$. Previous estimates for the total magnetization of rocks in the lower crust required to account for long-wavelength anomalies is 1.5–2.5 A m$^{-1}$ (Mayhew *et al.* 1991).

Magnetic scans were made in the NRM state, and after AF demagnetization to 80 mT. The magnetic mineralogy was correlated with the coercivity estimates from FORC diagrams, and from coercivity unmixing with the magnetic signals mapped by SMM. The ultramafic CS dunites and Upper Layered Series samples both contain an Al-chromite phase with exsolved Cr-magnetite microstructures of submicron to ∼40 μm sizes. The smallest exsolution size may account for the stable SD carriers in these rocks. The ULS rocks, and to lesser extent CS rocks contain clinopyroxene with exsolved magnetite lamellae as blades, which are also interpreted to be a stable magnetic carrier. Both the pyroxenite dyke and marginal zone samples also contain abundant fine exsolution lamellae of magnetite in the clinopyroxene. In addition, these samples showed abundant vortex and MD states which we correlate with the discrete magnetite grains, and larger exsolution lamellae of magnetite usually with blade morphology, from clinopyroxene.

The ultramafic samples discussed here have primary magnetic carriers, both Cr-magnetite and magnetite, that formed during the cooling of the complex. The high-coercivity grains would be a stable source of magnetization at depths in the crust when temperatures are below their respective Curie and blocking temperatures. RUC is proposed to represent the roots of a LIP and as such we would predict that the roots of other LIPs would also contain primary magnetic mineralogy, which may be stable at the appropriate pressure and temperatures. Based on these observations, we conclude that the remanent component of RUC should be sufficiently stable to measurably contribute to lithospheric anomalies..

## ACKNOWLEDGMENTS

Low temperature magnetic measurements were made at the Institute for Rock Magnetism (IRM) at the University of Minnesota. The IRM is a US National Multi-user Facility supported through the Instrumentation and Facilities program of the National Science Foundation, Earth Sciences Division, and by funding from the University of Minnesota. Magnetic measurements and SEM data were funded by NTNU. AK is thanked for the measurements on SQUID microscope. SM and HO are partly supported by JSPS Invitational Fellowship No. S16128 and JSPS KAKENHI grant no. 21H04523, respectively.

## DATA AVAILABILITY

The data related to the paper are available at DataverseNO (https://doi.org/10.18710/BQOL1B.

## REFERENCES

Balsley, J.R. & Buddington, A.F., 1958. Iron-titanium oxide minerals, rocks, and aeromagnetic anomalies of the Adirondack area, New York,. *Econ. Geol.,* **53**(7), 777–805.

Bennett, M.C., Emblin, S.R., Robins, B. & Yeo, W.J.A., 1986. High-temperature ultramafic complexes in the north Norwegian Caledonides: I—regional setting and field relationships. *Norges Geologiske Undersokelse,* **405,** 1–40.

Brown, L.L. & McEnroe, S.A., 2008. Magnetic properties of Anorthosites: a forgotten source for planetary magnetic anomalies?, *Geophys. Res. Lett.,* **35**(2), doi:10.1029/2007GL032522

Brown, L.L., McEnroe, S.A., Peck, W.H. & Nilsson, L.P., 2011. Anorthosites as sources of magnetic anomalies, in *The Earth's Magnetic Interior,* IAGA Special Sopron Book Series 1, pp. 321–342, eds Petrovsky´, E., Herrero-Bervera, E., Harinarayana, T. & Ivers, D., Springer.

Burton, B.P., Robinson, P., McEnroe, S.A., Fabian, K. & Boffa Ballaran, T., 2008. A low-temperature phase diagram for ilmenite-rich compositions in the system $Fe_2O_3$-$FeTiO_3$, *Am. Mineral.,* **93**(8-9), doi:10.2138/am.2008.2690.

Church, N. S. & McEnroe, S., 2018. Magnetic Field Surveys of Thin Sections. *ASEG Extended Abstracts,* **1**(1-5). doi: 10.1071/ASEG2018abW10_3F.

Church, N.S., Fabian, K. & McEnroe, S.A., 2016. Nonlinear Preisach maps: detecting and characterizing separate remanent magnetic fractions in complex natural samples. *J. geophys. Res.,* **121**(12), 8373–8395.

Clark, D.A., 1997 Magnetic petrophysics and magnetic petrology: aids to geological interpretation of magnetic surveys. *AGSO J. Aust. Geol. Geophys.,* **16**(1-2), 161–166. https://ecat.ga.gov.au/geonetwork/srv/api/records/fae9173a-71b4-71e4-e044-00144fdd4fa6.

Clark, D.A., 1999. Magnetic petrology of igneous intrusions: implications for exploration and magnetic interpretation. *Explor. Geophys.,* **30**(2), 5–26.

Day, R., Fuller, M. & Schmidt, V.A., 1977. Hysteresis properties of titanomagnetites: grain-size and compositional dependence. *Phys. Earth planet. Inter.,* **13**(4), 260–267.

de Groot, L.V., Fabian, K., Béguin, A., Reith, P., Barnhoorn, A. & Hilgenkamp, H., 2018 Determining individual particle magnetizations in assemblages of micrograins. *Geophys. Res. Lett.,* **45,** 2995–3000.

Dunlop, D.J. & Özdemir, Ö., 1997. *Rock Magnetism*. Cambridge Univ. Press.

Dunlop, D.J., Özdemir, Ö. & Costanzo-Alvarez, V., 2010. Magnetic properties of rocks of the Kapuskasing uplift (Ontario, Canada) and origin of long-wavelength magnetic anomalies. *Geophys. J. Int.,* **183**(2), 645–658.

Egli, R. & Heller, F., 2000. High-resolution imaging using a high-Tc superconducting quantum interference device (SQUID) magnetometer. *J. geophys. Res.,* **105**(B11), 25 709–25 727.

Egli, R., 2003. Analysis of the field dependence of remanent magnetisation curves. *J. geophys. Res.,* **108**(B2), 335–325.

Egli, R., 2004. Characterization of individual rock magnetic components by analysis of remanence curves, 1. Unmixing natural sediments. *Stud. Geophys. Geod.,* **48**(2), 391–446.

Egli, R., 2013. VARIFORC: an optimized protocol for calculating non-regular first-order reversal curve (FORC) diagrams. *Global planet. Change,* **110**(PC), 302–320.

Fabian, K. & Dobeneck, Von, T., 1997. Isothermal magnetisation of samples with stable Preisach function: a survey of hysteresis, remanence, and rock magnetic parameters. *J. geophys. Res.,* **102**(B8), 17 659–17 677.

Fabian, K., 2003. Some additional parameters to estimate domain state from isothermal magnetisation measurements. *Earth planet. Sci. Lett.,* **213**(3-4), 337–345.

Fabian, K., Shcherbakov, V.P. & McEnroe, S.A., 2013. Measuring the Curie temperature. *Geochem. Geophys. Geosyst.,* **14,** 947–961.

Ferré, E.C., Friedmanm, S.A., Martín-Hernández, F., Feinberg, J.M., Till, J.L., Ionov, D.A. & Conder, J.A., 2014. Eight good reasons why the uppermost mantle could be magnetic. *Tectonophysics,* **624–625,** 3–14.

Ferré, E.C., Kupenko, I., Martín-Hernández, F., Ravat, D. & Sanchez-Valle, C., 2021 Magnetic sources in the Earth's mantle. *Nat. Rev. Earth Environ.,* **2,** 59–69.

Gilder, S.A. & Le Goff, M., 2008. Systematic pressure enhancement of titanomagnetite magnetization. *Geophys. Res. Lett.,* **35**(6), doi:10.1029/2008GL033325.

Gilder, S.A., LeGoff, M., Chervin, J.-C. & Peyronneau, J., 2004. Magnetic properties of single and multi-domain magnetite under pressures from 0 to 6 GPa, *Geophys. Res. Lett.,* **31**(10), doi:10.1029/2004GL019844.

Grant, T., Larsen, R., Brown, E., Müller, A. & McEnroe, S.A., 2020. Mixing of heterogeneous, high-MgO, plume-derived magmas at the base of the crust in the Central Iapetus Magmatic Province (Ma 610-550): origin of parental magmas to a global LIP event. *Lithos,* **364-365,** doi:10.1016/j.lithos.2020.105535.

Grant, T.B. *et al.*, 2016. Anatomy of a deep crustal volcanic conduit system; the Reinfjord Ultramafic Complex, Seiland Igneous Province, Northern Norway. *Lithos,* **252-253(C),** 200–215.

Griffin, W.L., Sturt, B.A., O'Neill, C.J., Kirkland, C.L. & O'Reilly, S.Y., 2013. Intrusion and contamination of high-temperature dunitic magma: the Nordre Bumandsfjord pluton, Seiland, Arctic Norway. *Contrib. Mineral. Petrol.,* **165**(5), 903–930.

Hankard, F., Gattacceca, J., Fermon, C., Pannetier-Lecoeur, M., Langlais, B., Quesnel, Y., Rochette, P. & McEnroe, S.A., 2009. Magnetic field microscopy of rock samples using a Giant Magneto resistance-based scanning magnetometer. *Geochem. Geophys. Geosyst.,* **10**(10), doi:10.1029/2009GC002750.

Harrison, R.J. & Feinberg, J.M., 2008. FORCinel: an improved algorithm for calculating first-order reversal curve distributions using locally weighted regression smoothing. *Geochem. Geophys. Geosyst.,* **9**(5), doi:10.1029/2008GC001987.

Heslop, D., Dekkers, M.J., Kruiver, P.P. & Van Oorschot, I.H.M., 2002. Analysis of isothermal remanent magnetisation acquisition curves using the expectation-maximization algorithm. *Geophys. J. Int.,* **148**(1), 58–64.

Heslop, D., McIntosh, G. & Dekkers, M.J., 2004. Using time- and temperature-dependent Preisach models to investigate the limitations of modelling isothermal remanent magnetisation acquisition curves with cumulative log Gaussian functions. *Geophys. J. Int.,* **157**(1), 55–63.

Jackson, M.J. & Moskowitz, B.M., 2021. On the distribution of Verwey transition temperatures in natural magnetites. *Geophys. J. Int.,* **224**(2), 1314–1325.

Kawai, J., Oda, H., Fujihira, J., Miyamoto, M., Miyagi, I. & Sato, M., 2016. SQUID microscope with hollow-structured cryostat for magnetic field imaging of room temperature samples. *IEEE Trans. Appl. Supercond.,* **26**(5), 1–5.

Kelso, P.R., Banerjee, S.K. & Teyssier, C., 1993. Rock magnetic-properties of the Arunta Block, Central-Australia, and their implication for the interpretation of long-wavelength magnetic-anomalies. *J. geophys. Res.,* **98**(B9), 15 987–15 999.

Korhonen, J., Fairhead, P.J.D. & Hamoudi, M., 2007. *World Digital Magnetic Anomaly Map,* 1st edn, CCGM-CGMW/UNESCO.

Kruiver, P.P., Dekkers, M.J. & Heslop, D., 2001. Quantification of magnetic coercivity components by the analysis of acquisition curves of isothermal remanent magnetisation, *Earth planet. Sci. Lett.,* **189,** 269–276.

Kupenko, I. *et al.*, 2019. Magnetism in cold subducting slabs at mantle transition zone depths. *Nature,* **570,** 102–106.

Larsen, R.B.E. *et al.*, 2018. Portrait of a giant deep-seated magmatic conduit system: the Seiland Igneous Province. *Lithos,* **296-299(C),** 600–622.

Lee, M.D., McEnroe, S., Pastore, Z., Church, N. & Schmidt, P., 2023. Microscale magnetic inversion of remanent magnetization mineral sources from the Black Hill Norite, South Australia. *Geochem. Geophys. Geosyst.,* **24,** e2022GC010796.

Lima, E.A. & Weiss, B.P., 2016. Ultra-high sensitivity moment magnetometry of geological samples using magnetic microscopy. *Geochem. Geophys. Geosyst.,* **17**(9), 3754–3774.

Liu, Q., Frost, B.R., Hongcai, W., Zheng, J. & Zeng, Q., 2012. Magnetic petrology of high Fe-Ti eclogites from the CCSD main hole: implications for subduction-zone magnetism, *J. geophys. Res.,* **117**(B7), doi:10.1029/2011JB008621.

Maxbauer, D.P., Feinberg, J.M. & Fox, D.L., 2016. MAX UnMix_ A web application for unmixing magnetic coercivity distributions. *Comput. Geosci.,* **95(C),** 140–145.

Mayhew, M., Wasileski, P. & Johnson, B., 1991. Crustal magnetization and temperature at depths beneath the Yilgarn block, Western Australia inferred from Magsat data, *Earth planet. Sci. Lett.,* **107**(3-4), 515–522.

McEnroe, S.A., Brown, L.L. & Robinson, P., 2009. Remanent and induced magnetic anomalies over a layered intrusion: effects from crystal fractionation and recharge events, *Tectonophysics,* **478,** 119–134.

McEnroe, S.A., Harrison, R., Robinson, P., Golla, U. & Jercinovic, M.J., 2001a. The effect of fine-scale microstructures in titanohematite on the acquisition and stability of NRM in granulite facies metamorphic rocks from southwest Sweden: implications for crustal magnetism. *J. geophys. Res.,* **106,** 30 523–30 546.

McEnroe, S.A., Langenhorst, F., Robinson, P., Bromiley, G. & Shaw, C., 2004a. What is magnetic in the lower crust? *Earth planet. Sci. Lett.,* **226,** 175–192.

McEnroe, S.A., Robinson, P. & Panish, P., 2001b. Aeromagnetic anomalies, magnetic petrology and rock magnetism of hemoilmenite- and magnetite-rich cumulates from the Sokndal Region, South Rogaland, Norway. *Am. Mineral.,* **86**(11–12), 1447–1468.

McEnroe, S.A., Robinson, P. & Panish, P.T., 1996. Rock magnetic properties, oxide mineralogy, and mineral chemistry in relation to aeromagnetic interpretation and search for ilmenite reserves. Geological Survey of Norway Report 96.060.

McEnroe, S.A., Robinson, P., Church, N. & Purucker, M., 2018. Magnetism at depth: a view from an ancient continental subduction and collision zone. *Geochem. Geophys. Geosyst.,* **19,** 1123–1147.

McEnroe, S.A., Robinson, P., Langenhorst, F., Frandsen, C., Terry, M.P. & Boffa Ballaran, T., 2007. Magnetization of exsolution intergrowths of hematite and ilmenite: mineral chemistry, phase relations, and magnetic properties of hemo-ilmenite ores with micron- to nanometer-scale lamellae from Allard lake, Quebec, *J. geophys. Res.,* **112**(B10), doi:10.1029/2007JB004973.

McEnroe, S.A., Skilbrei, J.R., Robinson, P., Heidelbach, F., Langenhorst, F. & Brown, L.L., 2004b. Magnetic anomalies, layered intrusions and Mars, *Geophys. Res. Lett.,* **31**(19), doi:10.1029/2004GL020640.

Michels, A.C., McEnroe, S.A. & Fichler, C., 2018. Geophysical expression of the Leka Ophiolite, Norway modeled from integrated gravity, magnetic and petrophysical data. *Norw. J. Geol.,* **98,** 103–125.

Moskowitz, B.M., Frankel, R.B. & Bazylinski, D.A., 1993. Rock magnetic Criteria for the detection of biogenic magnetite. *Earth planet. Sci. Lett.,* **120**(3-4), 283–300.

Néel, L., 1955. Some theoretical aspects of rock-magnetism. *Adv. Phys.,* **4**(14), 191–243.

Oda, H. *et al.*, 2011. Ultrafine-scale magnetostratigraphy of marine ferromanganese crust. *Geology,* **39,** 227–230.

Oda, H. *et al.*, 2016. Scanning SQUID microscope system for geological samples: system integration and initial evaluation. *Earth Planets Space,* **68**(1), 1–19.

Pastore, Z., Church, N. & McEnroe, S.A., 2019. Multi-step parametric inversion of scanning magnetic microscopy data for modeling magnetisation of multidomain magnetite, *Geochem. Geophys. Geosyst.,* **20**(11), 5334–5351.

Pastore, Z., Fichler, C. & McEnroe, S.A., 2016. The deep crustal structure of the mafic-ultramafic Seiland Igneous Province of Norway from 3D gravity modeling and geological implications. *Geophys. J. Int.,* **207**(3), 1653–1666.

Pastore, Z., Fichler, C. & McEnroe, S.A., 2018a. Magnetic anomalies of the mafic/ultramafic Seiland Igneous Province. *Norw. J. Geol.,* **98,** 79–101.

Pastore, Z., Lelievre, P., McEnroe, S.A. & Church, N.S., 2022. 3D Joint inversion of scanning magnetic microscopy data. *Geophys. Res. Lett.,,* **49**(1), e2021GL096072.

Pastore, Z., McEnroe, S.A., Church, N. & Oda, H., 2021. Mapping and modelling mineral sources of natural remanent magnetisation from the Russell Belt microcline-sillimanite gneiss, Northwest Adirondack Mountains, USA. *Geochem. Geophys. Geosyst.,* **22**(3), doi:10.1029/2020GC009580.

Pastore, Z., McEnroe, S.A., ter Maat, G., Oda, H., Church, N. & Fumagalli, P., 2018b. Mapping magnetic sources at the millimeter to micrometer scale in dunite and serpentinite by high-resolution magnetic microscopy. *Lithos,* **323,** 174–190.

Pilkington, M. & Percival, J.A., 2001. Relating crustal magnetisation and satellite-altitude magnetic anomalies in the Ungava peninsula, northern Quebec, Canada. *Earth planet. Sci. Lett.,* **194**(1-2), 127–133.

Purucker, M.E. & Clark, D.A., 2011. Mapping and interpretation of the lithospheric magnetic field, in *Geomagnetic Observations and Models,* pp. 311–337, eds Mandea, M. & Korte, M., Springer.

Purucker, M.E. & Whaler, K.A., 2015. Crustal magnetism, in *Treatise on Geophysics,* 1st edn, Vol. **5,** pp. 185–218, ed. Kono, M., Elsevier.

Regan, R.D., Cain, J.C. & Davis, W., 1975. A global magnetic anomaly map. *J. geophys. Res.,* **80,** 794–802.

Roberts, A.P. *et al.*, 2019. Domain state diagnosis in rock magnetism: evaluation of potential alternatives to the Day diagram. *J. geophys. Res.,* **124,** 5286–5314.

Roberts, A.P., Heslop, D., Zhao, X. & Pike, C.R., 2014. Understanding fine magnetic particle systems through use of first-order reversal curve diagrams. *Rev. Geophys.,* **52**(4), 557–602.

Roberts, A.P., Tauxe, L., Heslop, D., Zhao, X. & Jiang, Z., 2018. A critical appraisal of the "day" diagram. *J. geophys. Res.,* **123**(4), 2618–2644.

Robertson, D.J. & France, D.E., 1994. Discrimination of remanence-carrying minerals in mixtures, using isothermal remanent magnetisation acquisition curves. *Phys. Earth planet. Inter.,* **82**(3), 223–234.

Robinson, P., Harrison, R.J. & McEnroe, S.A., 2006. $Fe^{2+}/Fe^{3+}$ charge ordering in contact layers of lamellar magnetism: bond valence arguments, *Am. Mineral.,* **91,** 67–72.

Robinson, P., McEnroe, S.A., Miyajima, N., Fabian, K. & Church, N., 2016. Remanent magnetisation, magnetic coupling, and interface ionic configurations of intergrown rhombohedral and cubic Fe-Ti oxides: a short survey. *Am. Mineral.,* **101**(3), 518–530.

Ryan, E.J., Sørensen, B.E., Drivenes, K. & Larsen, R.B., 2022. Infiltration of volatile-rich mafic melt in lower crustal peridotites provokes lower crustal earthquakes, *J. Struct. Geol.,* **163,** doi:10.1016/j.jsg.2022.104708.

Sabaka, T.J., Tøffner-Clausen, L., Olsen, N. & Finlay, C.C., 2020. CM6: a comprehensive geomagnetic field model derived from both CHAMP and Swarm satellite observations. *Earth Planets Space,* **72,** 80.

Schlinger, C.M., 1985. Magnetization of lower crust and interpretation of regional magnetic anomalies: example from Lofoten and Vesterålen, Norway. *J. geophys. Res.,* **90,** B13 11 484–11 504.

Schmidt, P.W., McEnroe, S.A., Clark, D.A. & Robinson, P., 2007. Magnetic properties and potential field modeling of the Peculiar Knob metamorphosed iron formation, South Australia: an analog for the source of the intense Martian magnetic anomalies?, *J. geophys. Res.,* **112**(B3), doi:10.1029/2006JB004495.

Schult, A., 1970. Effect of pressure on the Curie temperature of titanomagnetites $(1\text{-}x)Fe_3O_4 x Fe_2TiO_4$. *Earth planet Sci. Lett.,* **10,** 81–86.

Smirnov, A.V., 2009. Grain size dependence of low-temperature remanent magnetisation in natural and synthetic magnetite: experimental study. *Earth Planets Space,* **61**(1), 119–124.

Stevens, R.E., 1944. Composition of some chromites of the Western Hemisphere. *Am. Mineral.,* **29,** 1–34. https://pubs.geoscienceworld.org/msa/ammin/article-abstract/29/1-2/1/538515/Composition-of-some-chromites-of-the-Western.

Stockhausen, H., 1998. Some new aspects for the modelling of isothermal remanent magnetisation acquisition curves by cumulative log Gaussian functions. *Geophys. Res. Lett.,* **25**(12), 2217–2220.

Tauxe, L., Bertram, H.N. & Seberino, C., 2002. Physical interpretation of hysteresis loops: micromagnetic modeling of fine particle magnetite. *Geochem. Geophys. Geosyst.,* **3**(10), 1–22.

Tauxe, L., Mullender, T.A.T. & Pick, T., 1996. Potbellies, wasp-waists, and superparamagnetism in magnetic hysteresis. *J. geophys. Res.,* **101,** 571–583.

ter Maat, G.W., McEnroe, S.A., Church, N.S. & Larsen, R.B.E., 2019. Magnetic mineralogy and petrophysical properties of Ultramafic Rocks: consequences for crustal magnetism, *Geochem. Geophys. Geosyst.,* **20**( 4), 1794–1817.

Thébault, E. *et al.*, 2015. International Geomagnetic Reference Field: the 12th generation. *Earth Planets Space,* **67**(1), 68–19.

Walz, F., 2002. The Verwey transition—a topical review. *J. Phys. Condens. Matter,* **14**(12), R285–R340.

Wang, D. & Van der Voo, R., 2004. The hysteresis properties of multidomain magnetite and titanomagnetite/titanomaghemite in mid-ocean ridge basalts. *Earth planet. Sci. Lett.,* **220**(1-2), 175–184.

Weiss, B.P., Lima, E.A., Fong, L.E. & Baudenbacher, F.J., 2007. Paleomagnetic analysis using SQUID microscopy. *J. geophys. Res.,* **112**(B9), 11715–11720.

Yu, Y. & Tikoff, B., 2020. Magnetic Cr-rich spinel in serpentinized ultramafic complexes, *J. geophys. Res.,* **125,** e2020JB020443, doi:10.1029/2020JB020443.